

# **Investigating the Role of Secondary Inlets in Valved Holding Chamber Drug Delivery**

**by  
Anahita Sayyar**

B.A.Sc., Amirkabir University of Technology, 2016

Thesis Submitted in Partial Fulfillment of the  
Requirements for the Degree of  
Master of Applied Science

in the  
School of Mechatronic Systems Engineering  
Faculty of Applied Sciences

© Anahita Sayyar 2021  
SIMON FRASER UNIVERSITY  
Fall 2021

Copyright in this work rests with the author. Please ensure that any reproduction or re-use is done in accordance with the relevant national copyright legislation.

## Declaration of Committee

**Name:** Anahita Sayyar

**Degree:** Master of Applied Science

**Title:** Investigating the Role of Secondary Inlets in Valved Holding Chamber Drug Delivery

**Committee:**

**Chair:** Amr Marzouk  
Senior Lecturer, Mechatronic Systems Engineering

**Siamak Arzanpour**  
Supervisor  
Associate Professor, Mechatronic Systems Engineering

**Mehrab Ahmadi**  
Committee Member  
Lecturer, Sustainable Energy Engineering

**Hellen Bailey**  
Examiner  
Lecturer, Mechatronic Systems Engineering

## Abstract

Asthma and Chronic Obstructive Pulmonary Disease (COPD) are two well-known chronic lung diseases. Pressurized Metered Dose Inhaler (pMDI) is a popular treatment for asthma and COPD for its several advantages which include quick and easy to use, low cost, and pocketable size. However, pMDI has some limitations including particle deposition in the mouth and coordination between inhalation and pMDI actuation. These limitations can be addressed by using Valved Holding Chamber (VHC). A study compared the performance of eight VHCs, and the experimental result showed that PARI VORTEX® has the best performance in drug delivery in comparison with the other seven VHC. This thesis hypothesis is that the exceptional performance of PARI VORTEX® is related to its special designs that benefit from a unique pMDI adaptor that has four blades and secondary inlets.

Contributions of this thesis include the computational and experimental study of the role of secondary inlets on the VHC drug delivery and flow inside the VHC. The experimental and computational results indicated that the open secondary inlets increase the total drug delivery and decrease the average particle size at the outlet. Moreover, the blade's geometry and its inlet were optimized to improve the spacer's drug delivery. The outcome of this thesis can be used for developing the ideal VHC. Ideal VHC is defined as an add-on device that helps to minimize the drug deposition in the patient mouth and maximize the drug delivery to the patient's lung.

**Keywords:** Pressurized Metered Dose Inhaler (pMDI), Valved Holding Chamber (VHC), Asthma, Chronic Obstructive Pulmonary Disease (COPD), Computational Fluid Dynamic (CFD), Optimization, ANSYS

*I dedicate my thesis work to my supportive husband and my loving family. A special feeling of gratitude to my parents and my sister Shadi. I also dedicate this thesis to my husband who has supported me throughout the process and has never left my side. I will always appreciate all he has done.*

## **Acknowledgements**

I would like to express my deep and sincere gratitude to my supervisor Dr.Arzanpour for all his support and guidance during my research. His guidance helped me in all the time of research and writing this thesis. I could not have imagined having a better advisor and mentor for my research. I would like to take the opportunity to express my gratitude toward Shahab Azimi for his incredible depth of knowledge and support.

# Table of Contents

Declaration of Committee .....	ii
Abstract .....	iii
Dedication .....	iv
Acknowledgements .....	v
Table of Contents .....	vi
List of Tables .....	viii
List of Figures .....	ix
List of Acronyms .....	xi
<b>Chapter 1. Introduction .....</b>	<b>1</b>
1.1. Background of study .....	1
1.2. Research Objective .....	4
1.3. Thesis Outline .....	5
<b>Chapter 2. Literature Review .....</b>	<b>7</b>
2.1. Respiratory System .....	7
2.1.1. Introduction .....	7
2.1.2. Respiratory Disease .....	8
Asthma .....	8
COPD .....	9
2.1.3. Drug Deposition .....	11
Inertial Impaction .....	12
Brownian Diffusion .....	12
Gravitational Sedimentation .....	13
Electrostatic Deposition .....	13
Interception .....	14
2.2. Inhalation Devices .....	14
2.2.1. Pressurized Metered-Dose Inhaler(pMDI) .....	15
2.2.2. Spacer and Valved Holding Chamber (VHC) .....	17
2.2.3. Nebulizer .....	19
2.2.4. Dry Powder Inhaler .....	21
2.3. Conclusion .....	22
<b>Chapter 3. Numerical Study .....</b>	<b>23</b>
3.1. Introduction .....	23
3.2. Material and Method .....	23
3.2.1. Geometry and Mesh .....	24
3.2.2. Particle Modeling .....	27
Particle Tracking Modeling .....	27
Particle Breakup .....	28
Particle Distribution .....	31
Spray Simulation .....	33

3.2.3. Flow Modeling and Boundary Condition.....	33
Navier–Stokes Equations and Turbulence Model.....	33
Boundary Condition.....	39
3.3. Result and Discussion .....	39
3.3.1. Drug delivery .....	39
3.3.2. Velocity.....	42
3.4. Conclusion.....	48
<b>Chapter 4. Experimental Study.....</b>	<b>49</b>
4.1. Objective .....	49
4.2. Cascade Impactor .....	49
4.3. Experiment Setup and Procedure.....	50
4.4. Drug Collection and Measurement .....	52
4.4.1. Ultraviolet-Visible Spectrophotometer.....	53
4.5. Result and Discussion .....	55
4.6. Conclusion.....	57
<b>Chapter 5. Design Optimization .....</b>	<b>59</b>
5.1. Introduction.....	59
5.2. Optimization Method.....	59
5.2.1. Direct Optimization in ANSYS.....	59
5.3. Optimization Parameters .....	66
5.4. ANSYS Setup.....	67
5.5. Result and Discussion .....	69
5.6. Conclusion.....	74
<b>Chapter 6. Summery and Future Work .....</b>	<b>75</b>
6.1. Summery.....	75
6.2. Future Work.....	76
<b>References.....</b>	<b>77</b>

## List of Tables

Table 3-1 Breakup mode and Weber number range relation for $Oh < 0.1$ [96].....	30
Table 3-2 Breakup regime for Schmehl Breakup Model [99].....	31
Table 3-3 Rosin Rammler Parameters .....	32
Table 3-4 Drug Characteristic.....	33
Table 3-5 $\Phi_1$ and $\Phi_2$ value to calculate SST constants .....	38
Table 3-6 Salbutamol Mass Flow Rate in CSIS and OSIS.....	41
Table 3-7 Average Velocity on defined locations .....	45
Table 5-1 Optimization result.....	69



## List of Figures

Figure 1-1 Prevalence of diagnosed asthma among Canadians aged one year and older, by 10-year age group and year, Canada, 2000–2001 to 2011–2012. Reproduced [1] .....	1
Figure 1-2 Prevalence of diagnosed COPD among Canadians aged 35 years and older, by 10-year age group and year, Canada, 2000–2001 to 2011–2012. Reproduced [1] .....	2
Figure 1-3 World Map of the Prevalence of Clinical Asthma. Reproduced [2] .....	3
Figure 1-4 PARI VORTEX pMDI adaptor .....	5
Figure 2-1 Major Respiratory Structures [20] .....	8
Figure 2-2 Pathophysiology of asthma [25] .....	9
Figure 2-3 Comparisons between healthy and COPD bronchioles and alveoli [27] .....	10
Figure 2-4 a) Healthy alveoli B) COPD alveoli (hyperinflated) [28] .....	10
Figure 2-5 Schematic diagram of particle deposition in respiratory system [32] .....	11
Figure 2-6 Schematic of pressurized metered-dose inhaler[46] .....	16
Figure 2-7 Ricardo’s study a) twelve configurations of valve b) eight configurations of body design [67] .....	19
Figure 2-8 a) Jet Nebulizer b) Ultrasonic Nebulizer c) Vibrating-Mesh nebulizer .....	20
Figure 2-9 Vibrating mesh nebulizer mechanism schematic[79]. .....	21
Figure 3-1 a) VORTEX schematic and boundaries locations b) Coordination position in VORTEX .....	24
Figure 3-2 Comparisons of flow velocity a) centerline velocity of the spacer b) velocity along y-direction in inlet surface b) velocity along z-direction in inlet surface .....	26
Figure 3-3 Newtonian Particle Breakup Modes [97] .....	28
Figure 3-4 Numerical results for drug deposition in OSIS and CSIS .....	41
Figure 3-5 Plane 1 and Plane 2 locations in the Spacers .....	42
Figure 3-6 Velocity contour of a) OSIS in plane-1 b) CSIS in plane-1 c) OSIS in plane-2 d) CSIS in plane-2 .....	44
Figure 3-7 Velocity streamlines of a) OSIS in plane-1 b) CSIS in plane-1 c) OSIS in plane-1 d) CSIS in plane-2 .....	47
Figure 4-1 Anderson cascade impactor .....	50
Figure 4-2 CSIS Designed pMDI adaptor .....	51
Figure 4-3 Experiment setup for the effect of stator blades in particles size .....	52
Figure 4-4 a) Deposited drug in cascade impactor plate b) washing cascade impactor stage .....	53
Figure 4-5 Illustration UV-vis instrument [126] .....	53
Figure 4-6 a) Placing a sample into UV-Vis b) Agilent Cary 60 UV-Vis .....	55
Figure 4-7 Particle deposition fraction (recovered drug in each stage is divided by the total recovered drug in each spacer) in OSIS and CSIS. ....	56

Figure 4-8 Numerical and Experimental results for drug deposition in OSB and CSB spacers .....	57
Figure 5-1 Genetic Algorithm crossover operation types for discrete parameters .....	61
Figure 5-2 Genetic Algorithm mutation operation for discrete parameters .....	61
Figure 5-3 Multi-Objectives Genetic Algorithm workflow [128] .....	62
Figure 5-4 Non-dominated sorting for a multi-objective function [132] .....	63
Figure 5-5 NSGA-II workflow .....	64
Figure 5-6 Crowding distance Calculation for two objective functions [134] .....	65
Figure 5-7 Optimization Input parameters .....	67
Figure 5-8 Spacer number of secondary inlets relation with a) total drug delivery at outlet b) output particle average size .....	71
Figure 5-9 Secondary inlet height relation with a) total drug delivery at outlet% b) output particle average size[micron].....	72
Figure 5-10 Secondary inlet location relation with a) total drug delivery at outlet% b) output particle average size[micron].....	73
Figure 5-11 Secondary inlet corner angle relation with a) total drug delivery at outlet% b) output particle average size[micron].....	73

## List of Acronyms

CAB	Cascade Atomization Breakup
CCD	Central Composite Design
CCF	Central Composite Face-Centered Design
CFD	Computational Fluid Dynamic
CI	Cascade Impactor
CSIS	Closed secondary Inlet Spacer
DNS	Direct Numerical Simulation
DOE	Design of Experiment
DPI	Dried Powered Inhaler
ETAB	Enhanced Taylor Analogy Breakup
EFP	Extra Fine Particles
EFPP	Extra Fine Particles Percentage
FEV1	Forced Expiratory Volume in the first second
FP	Fine Particles
FPP	Fine Particles Percentage
FVC	Forced Vital Capacity
HPLC	High-Performance Liquid Chromatography
IP	Induction's Port
LD	Laser Diffraction
LES	Large Eddy Simulation
MDI	Metered Dose Inhaler
MISQP	Mixed-Integer Sequential Quadratic Programming
MMAD	Mass Median Aerodynamic Diameter
MMPA	Mass Median Plume Angle
MOGA	Multi-Objective Genetic Algorithm
MSIL	Multistage Liquid Impinger
MT	Mouth-Throat (MT)
NGI	New Generation Impactor
NLPQL	Nonlinear Programming by Quadratic Lagrangian
OSIS	Open Secondary Inlet Spacer
OSF	Optimal Space-Filling Design
PDA	Phase Doppler Anemometry
PET	Polyethylene Terephthalate
PIPE	Plume Induction Port Evaluator
PTEF	Polytetrafluoroethylen
pMDI	Pressurized Metered Dose Inhaler
RANS	Reynolds Averaged Navier-Stokes

RSM	Respond Surface Method
SAINT	Sophia Anatomical Infant Nose-Throat
SGS	Sub-Grid Scale
SEM	Scanning Electron Microscope
TAB	Taylor Analogy Breakup
UV-Vis	Ultraviolet-Visible Spectrophotometry
VHC	Valved Holding Chamber

# Chapter 1.

## Introduction

### 1.1. Background of study

Asthma and chronic obstructive pulmonary disease (COPD) are two well-known chronic lung diseases [1]. The inflamed and narrowed airways in asthma cause shortness of breath, wheezy inhalation, and chest tightness. Coughing and shortness of breath are common symptoms of COPD. COPD has been mainly diagnosed in tobacco smokers and second-hand smokers. However, the reason for asthma has not been discovered yet.

The Canadian Chronic Disease Surveillance System (CCDSS) reported that 3.8 million Canadians older than one year suffered from asthma in 2011-2012 [2]. They also stated 2 million 35 years, or older Canadians suffered from COPD during 2011-2012. The asthmatic and COPD Canadian patients have been shown in Figure 1-1 and Figure 1-2, respectively.

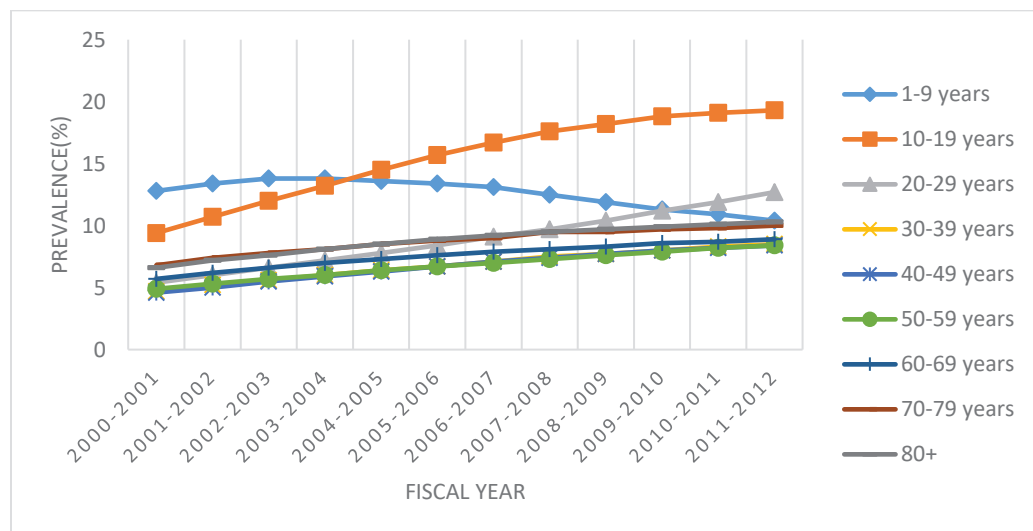


Figure 1-1 Prevalence of diagnosed asthma among Canadians aged one year and older, by 10-year age group and year, Canada, 2000–2001 to 2011–2012. Reproduced [1]

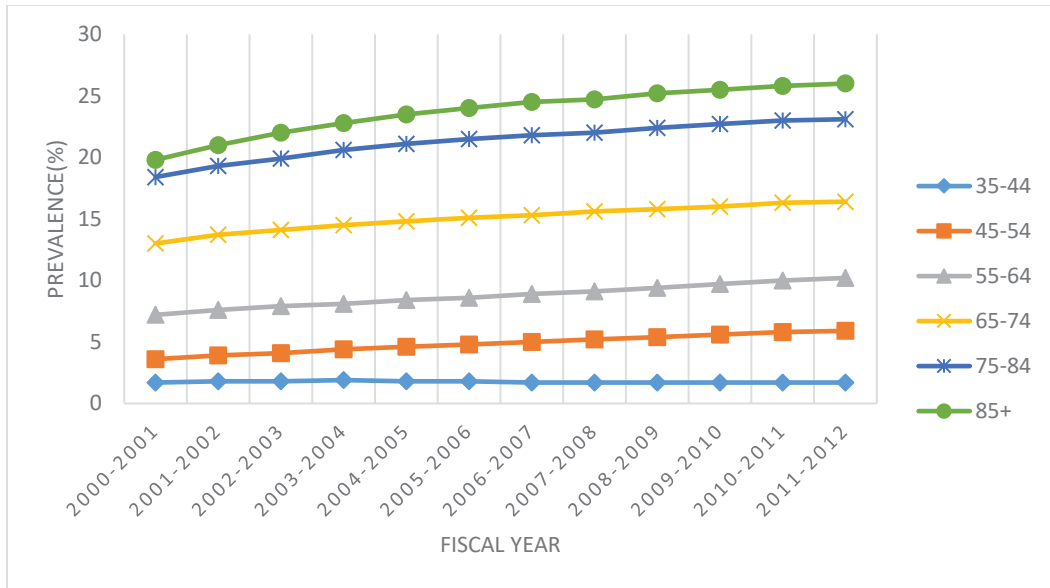


Figure 1-2 Prevalence of diagnosed COPD among Canadians aged 35 years and older, by 10-year age group and year, Canada, 2000–2001 to 2011–2012. Reproduced [1]

Figure 1-1 and Figure 1-2 show asthma and COPD rates have been increased between 2000-2012. Moreover, Figure 1-1 represents the line slope increased in group age 10-19 which indicates the growth rate is higher in this age group.

Chronic lung diseases are not unique to Canada. Masoli et al.(2004)[2] studied patients who suffer from asthma around the world. They gathered data from more than 84 countries and sorted countries based on the highest rate of asthma in the population to the lowest rate. Scotland held 1st place where more than 18% of the Scottish population were diagnosed with asthma. England, New Zealand, and Australia ranked as 5<sup>th</sup>, 6<sup>th</sup>, and 7<sup>th</sup> respectively. Canada was ranked 10<sup>th</sup> on the list. Data indicated that more than 10% of American, Canadian, and Australian populations suffer from Asthma (Figure 1-3).

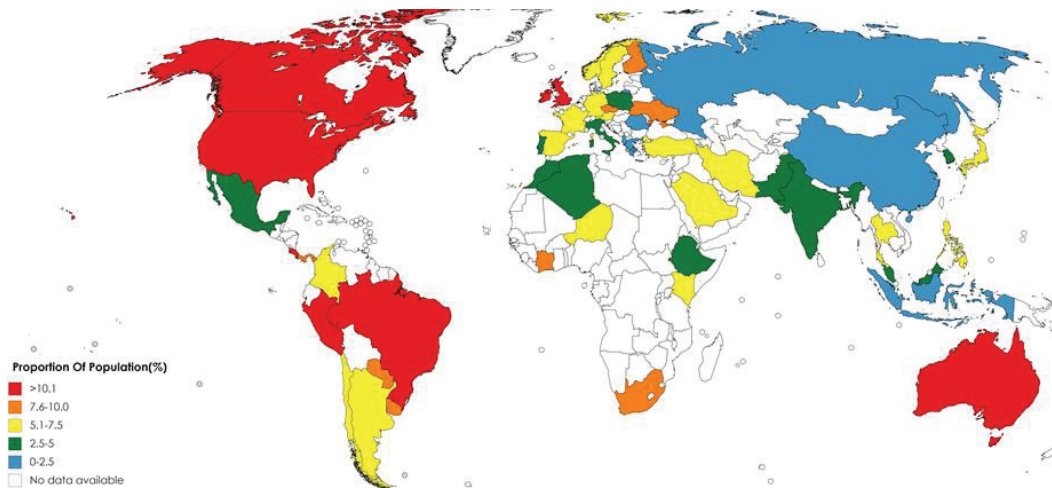


Figure 1-3 World Map of the Prevalence of Clinical Asthma. Reproduced [2]

Asthma and COPD treatment methods can be categorized into two groups: long-term treatment and quick relief [3]. The long-term treatment focuses on controlling and preventing the disease's symptoms. The treatment can be delivered to a patient through inhalation devices, pills, injections, and syrups. On the other hand, quick treatment focuses on symptom alleviation. Quick-term treatment medicines are delivered to the patient's lung using only inhalation devices. In fact, inhalation devices use airways to deliver the drug to the patient's respiratory system, and they can be used for both long-term and quick-relief treatments.

There are several inhaled treatments for chronic lung diseases such as Pressurized Metered Dose Inhaler (pMDI), Dried Powder Inhaler (DPI), soft mist inhalers, and Nebulizer. pMDI is an inhalation device that releases the drug as a form of spray when it is actuated [4]. While DPI is an inhalation device that requires deep inhalation flow to release the drug. Soft mist is a new inhaler device generation that releases a cloud of a drug instead of spraying form. The main difference between the spray form and the mist form is the particle's velocity, and the mist form consists of lower velocity particles than the spray form. Similar to soft mist inhaler, Nebulizer delivers medicine to a patient's respiratory system by generating a mist of medication, but the mist contains a lesser amount of medication in comparison with a soft mist inhaler [4].

Several studies have shown the advantages of pMDI over other inhalation devices for the treatment of asthma and COPD [5]-[7]. Lavorini et. al., [5] compared the sale quantity of three different inhalation devices including pMDI, DPI, and Nebulizer. The study concluded that the sales of pMDI were highest in Europe in comparison with two other devices due to its low cost and pocketable. Another study posited that pMDI is a desirable choice for emergency treatment because it is quick in drug delivery and easy to use [6]. Furthermore, the device is designed to deliver a consistent dose of a drug to the patient's respiratory system from the first puff to the last puff [7]. Overall, the advantages of pMDI make it popular for asthma treatment.

Although pMDI has several advantages over other inhalation devices, it has some limitations. Coordination between inhalation and injecting a puff to the mouth is needed [8]. If the patient fails to synchronize her/his inhalation with drug injection, the amount of delivered drug to the lung will be changed. Therefore, the patient may not receive the prescribed doses. Furthermore, elderly or children can not properly coordinate spray actuation with inhaling [9]. Another problem that pMDI users may face is the particles deposition in the mouth [10]. This problem can be associated with side effects such as reducing children's growth rate [11].

These problems can be addressed by using a device which is called a spacer. The spacer is an add-on medical device that has an inhaler adaptor on one side to place the pMDI and a mouthpiece on the other side that patient places it into her/his mouth. The patient sprays the drug into the spacer and then inhales through this add-on device. The main advantage of the spacer is to reduce the drug deposition in the mouth. However, the spacer has a limitation that does not prevent patient exhalation toward the inside of the spacer. To address the issue, the spacers have been equipped with a one-way valve close to the opening of the mouthpiece to prevent entering exhalation inside the spacer. Some articles used "valved holding chambers (VHC)" for these spacers to emphasize their difference to spacers without valves [12]–[14]. Studies showed that the pMDI drug delivery improves when it was used with spacer/VHC [15][16].

## **1.2. Research Objective**

It has been shown that the different VHC and spacers have different drug delivery [15][16]. It was claimed that the VHC geometry has a relationship with its output. Ricardo



et al. [17] compared several spacer/VHC efficacy and found that PARI VORTEX® has the highest drug delivery among seven other VHCs. It is believed that the exceptional performance of PARI VORTEX® is related to its special designs that benefit from a unique pMDI adaptor cap. The VORTEX pMDI adaptor cap has four static blades which are shown in Figure 1-4. Each of these static blades has a narrow inlet, through where air pass toward the spacer. In this thesis, we investigate the role of secondary inlets on the spacer drug delivery and flow inside the spacer. Later the blade's geometry and its inlet are optimized to improve the spacer's drug delivery. The outcome of this work can be used for developing the best VHC. Best VHC is defined as an add-on device that helps to minimize the drug deposition in the patient mouth and maximize the drug delivery to the patient's lung.



Figure 1-4 PARI VORTEX pMDI adaptor

### 1.3. Thesis Outline

The remainder of the thesis is structured as follows:

#### Chapter 2

First, the human respiratory system is succinctly explained. Then, summarized descriptions of Asthma and COPD are explained. Next, several inhalation treatments are discussed then their advantages and limitations are pointed out. The most recent research

related to computational simulation and experiment is explained in detail in chapters 3 and 4, respectively.

### Chapter 3

To investigate the role of the static blade in PARI Vortex drug delivery, we simulate the drug delivery of this spacer. The spacer is simulated in two modes: the static blades inlets are open and closed. Then the numerical result of these two setups is compared and the role of the static blades on drug particles is explained.

### Chapter 4

To verify the numerical study, an experimental study is conducted. During this study, the role of the static blades in PARI Vortex drug delivery is studied. Later in this chapter, the experimental and numerical results are compared.

### Chapter 5

The static blade geometry is optimized in this chapter. First, its geometry parameters are defined, and objective functions are introduced. Then the optimization result is compared with the original PARI Vortex design.

## Chapter 2.

### Literature Review

In this chapter, initially, the human respiratory system is explained, then it will be followed by a succinct explanation of asthma and COPD which are the two common respiratory diseases. Afterward, several inhalation treatments will be introduced and compared. In the end, the methods that are used to study inhalation devices' efficacy and performance will be discussed.

#### 2.1. Respiratory System

##### 2.1.1. Introduction

The main role of the respiratory system is to provide oxygen to the bloodstream and take carbon dioxide from the blood and release it into the air during exhalation. The respiratory system in humans (Figure 2-1) consists of nasal passages, pharynx, trachea, bronchus, bronchioles, alveolar duct, and alveolar [18]. The respiratory system can be divided into two parts: The conducting zone and the respiratory zone [19]. The conducting zone is composed of organs that are not directly engaged in oxygen delivery to blood. They aim to provide a passage for air in and out of the respiratory system. The respiratory zone includes organs that have the  $O_2-CO_2$  gas exchange role.

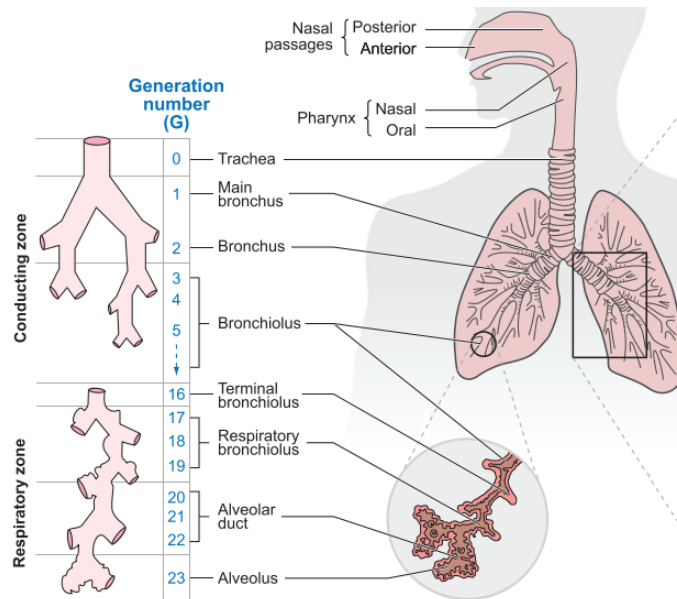


Figure 2-1 Major Respiratory Structures [20]

## 2.1.2. Respiratory Disease

### *Asthma*

Asthma is a disease in which the airway becomes narrower and may difficult breathing [19]. The trachea and bronchi of a person with asthma are inflamed all the time which in the presence of triggers the inflation becomes worst. Figure 2-2 shows a comparison between a healthy bronchial tube, asthmatic bronchial tube in normal circumstances and under attack. As it is shown in Figure 2-1, the bronchial tube is a part of conducting zone which provides a pathway for incoming and outgoing airflow. When the airways become narrower under attack, the ventilation is disrupted which may lead to an air trap in alveoli [21]. An asthma attack may be associated with wheezing, chest pain and coughing, etc. Asthma attacks can be avoided by controlling the airway inflation or restraining asthma triggers including but not limited to tobacco smoke, exercise, air pollutants, and respiratory infections [22].

According to the Forum of International Respiratory Societies, nearly 180'000 persons die in the world because of asthma [23]. Asthma usually onset in early childhood and only a small portion is adult-onset asthma [24]. Air pollution, genetic disorder, and allergens are well-known risk factors that enhance the chance of developing asthma.

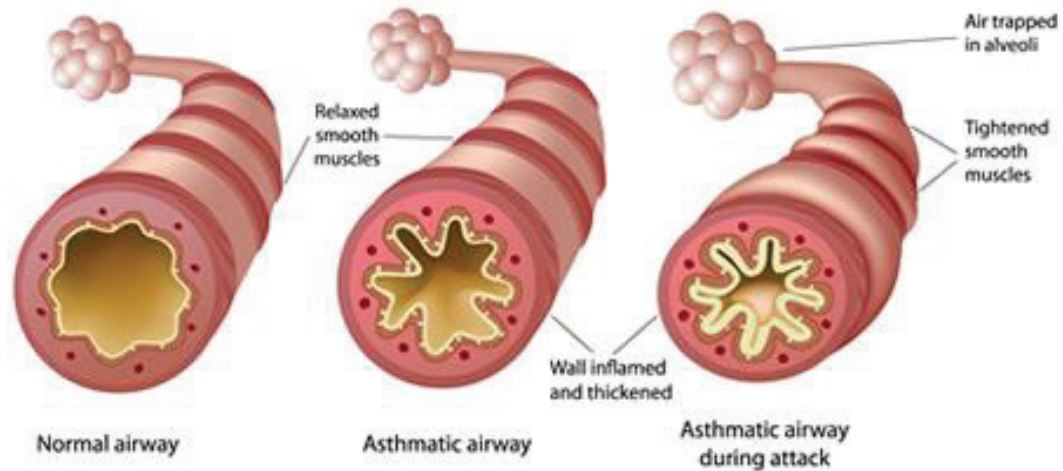


Figure 2-2 Pathophysiology of asthma [25]

## ***COPD***

Chronic obstructive pulmonary disease (COPD) is a lung disease that is currently incurable [26]. Studies characterized COPD by progressive airway obstruction that leads to shortness of breath and frequent coughing (COPD common symptoms) [21]-[24]. Damaged bronchioles and/or alveoli are the main characteristic of COPD [21]. As it is shown in Figure 2-3, the COPD bronchioles are inflamed and have extra mucus which may cause frequent coughing. Moreover, deformed alveoli may partially or completely lose their function which is exchanging O<sub>2</sub> and CO<sub>2</sub> [27]. Healthy alveoli consist of several air bags which share walls with their neighbor alveoli air bag [28]. COPD alveoli are hyperinflated which destroys alveoli walls. The air exchange surface reduction declines the alveoli air exchange capacity. Moreover, in a healthy lung, the pressure of collapsing airway in exhalation is balanced with the lung elasticity pressure which helps the airways to remain open [21]. The COPD's lung may lose its elasticity which resulted in imbalances between these two pressures. A comparison between healthy alveoli and COPD alveoli is shown in Figure 2-3 and Figure 2-4. As it is shown the alveoli are hyperinflated and the walls are destructed. Therefore, the respiratory zone may face poor ventilation.

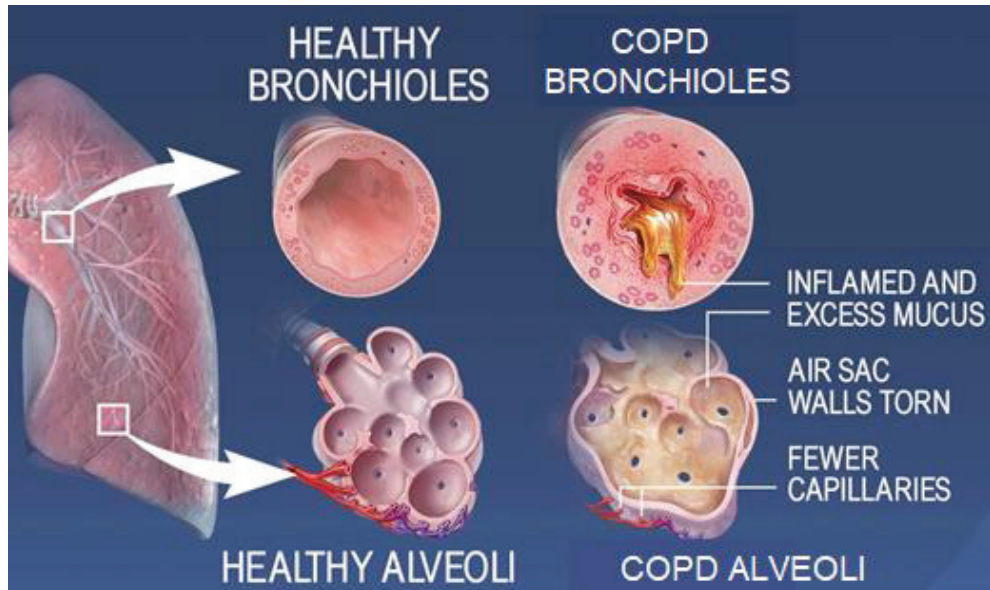


Figure 2-3 Comparisons between healthy and COPD bronchioles and alveoli [27]

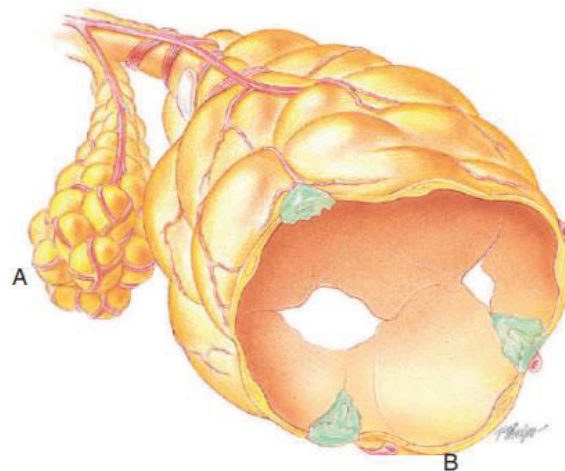


Figure 2-4 a) Healthy alveoli B) COPD alveoli (hyperinflated) [28]

COPD risk factors include genetic disorder, age, exposure to particles (tobacco smoke, organic and inorganic dust, chemical fumes, and air pollution), asthma, and respiratory infection [28]. There is no specific connection between age and COPD however it may be related to the person's exposures to the other risk factor throughout life. COPD symptoms can be controlled by avoiding COPD exacerbation which includes bacteria, viruses, and pollutants [29].

### 2.1.3. Drug Deposition

Inhalation medicine aims to deliver the drug directly to the desired locations. Understanding particle deposition helps to increase the drug delivery efficacy to the targeted area in the respiratory system. The drug delivery and particle deposition will be discussed in this section.

The inhaled particles are absorbed in the oropharynx or respiratory zone. The particle absorption may occur by the digestive system or respiratory system. The deposited particles in the oral region are swallowed and move toward the gastrointestinal tract. Gastrointestinal absorption occurs in this stage where the gastrointestinal tract metabolizes the swallowed drug particles [30]. However, this process has a delay in comparison with lung absorption [31]. It was observed that after 30 min of using the inhaler, only 0.3% of the injected drug was metabolized in the gastrointestinal tract [31]. Therefore, this thesis devotes its major attention to drug delivery to the lung.

Studies on drug delivery to the lung categorized particle deposition into five groups including inertial impaction, Brownian diffusion, gravitational sedimentation, electrostatic deposition, and interception [32]. Figure 2-5 shows these five deposition mechanisms on bronchial tube and alveoli regions.

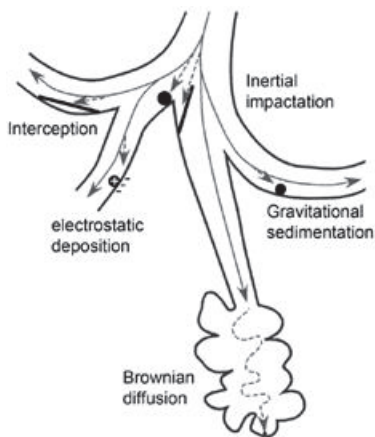


Figure 2-5 Schematic diagram of particle deposition in respiratory system [32]

In order to study particle behavior and deposition, the aerodynamic diameter needs to be defined first. Due to the non-spherical shape of aerosol particles, the *aerodynamic*



*diameter* parameter was defined to measure the irregular-shaped particle's size [33]. The aerodynamic diameter is the diameter of an imaginary spherical particle with a density of  $1g/cm^3$  which has the same settling velocity ( settling velocity is the terminal velocity of a particle in still fluid [34]) as the irregular particle [33]. Therefore, the aerodynamic diameter equals:

Equation 2-1

$$d_{ae} = d \times \sqrt{\frac{\rho}{\rho_0}}$$

Where  $d$ ,  $\rho$  and  $\rho_0$  represent the actual diameter, the actual density, and the unit density ( $1g/cm^3$ ) respectively.

### ***Inertial Impaction***

Inertial impaction occurs when the particle momentum is large enough to prevent the particle from changing its pathway same as the air stream [35]. Therefore, the particle doesn't follow the air stream and may collide with the airway wall. The Stokes' number is a dimensionless parameter to define the characteristics of particle deposition. The high Stokes' number represents the higher chance of particle deposition by the inertial impaction mechanism. The Stokes' number (*Stk*) equation is shown as follow:

Equation 2-2

$$Stk = \frac{\rho \cdot d_{ae}^2 \cdot u}{18 \cdot \eta \cdot R}$$

Where  $d_{ae}$  is particle aerodynamic diameter.  $u$  and  $\eta$  represent air mean velocity and dynamic viscosity respectively and  $R$  is airway radius [32]. The Stokes' number has a direct relationship with the aerodynamic diameter squared (Equation 2-2), which shows inertial impaction deposition chance is higher in larger particles.

### ***Brownian Diffusion***

The Browning diffusion (Brownian motion) is the random movements of a sufficiently small particle and its impaction with other particles and molecules in the fluid flow [32]. Stokes-Einstein equation defines the diffusion coefficient (Dif) as:

Equation 2-3



$$Dif = \frac{k.T}{3.\pi.\eta.d_{ae}}$$

Where k and T are Boltzmann's constant and absolute temperature respectively. Diffusion rate has a reverse relationship with the particle's aerodynamic diameter and fluid's dynamic viscosity. The Brownian diffusion is the primary deposition mechanism for the particle size smaller than  $0.5\mu m$  [35].

### **Gravitational Sedimentation**

Sedimentation happens due to gravity force acting on the particle and mostly occurs for particle size between  $1-8\mu m$  [35]. Particle settling velocity ( $V_s$ ) :

Equation 2-4

$$V_s = \frac{\rho \cdot d_{ae}^2 \cdot g}{18 \cdot \eta}$$

Where  $g$  represents gravitational acceleration. Deposition fraction is the ratio of deposited particles of a particular size to the total same size particles that entered the respiratory system [36]. Deposition fraction due to sedimentation ( $f_s$ ) in a horizontal tube with laminar flow is [35]:

Equation 2-5

$$f_s = \frac{2}{\pi} \left[ 2\varepsilon \sqrt{1 - \varepsilon^{\frac{2}{3}}} - \varepsilon^{\frac{1}{3}} \sqrt{1 - \varepsilon^{\frac{2}{3}}} + \arcsin \left( \varepsilon^{\frac{1}{3}} \right) \right]$$

$$\varepsilon = \frac{3V_s l}{4u d_{ae}} = \frac{\rho_p \cdot d_{ae} \cdot g \cdot l}{24 \cdot \eta \cdot u}$$

Where  $l$  represents the airway length. The sedimentation fraction has a nonlinear relationship with  $\varepsilon$  function. Particle settling velocity, aerodynamic diameter, and airway length increase enhance sedimentation deposition fraction.  $l/u$  parameter indicates that sedimentation is a time-dependent mechanism.

### **Electrostatic Deposition**

Aerosol particles have an electrostatic charge that is generated by particle friction impaction [35]. The *Image Charges*, which are usually induced on the small airways, attract drug particles with the opposite charge and cause deposition on the airway wall. Electrostatic deposition function ( $f_{E1}$ ) in a cylindrical tube with  $R$  radius is equal to:

Equation 2-6

$$f_{E1} = \frac{n_0 R^3 \tau}{1 + n_0 R^3 \tau}$$
$$\tau = \frac{Bq^2 l}{4\pi\epsilon_0 R^3 u}$$

Where  $n_0$  is particles' concentration in tube inlet, and  $\epsilon_0$  is air permittivity.  $B$  and  $q$  represent the particle mobility and charge respectively.

### **Interception**

Interception deposition occurs if elongated particles are close enough to the airway surface [35]. A particle is defined as elongated if its length ratio over the mean diameter is over 1.8 [37]. It was observed that if the elongated particle distance from a surface is less than a particle radius, it may be deposited on the wall [38]. Interception deposition probability has a direct relationship with particle length [39]. The average velocity of the deposited particle by interception mechanism is equal to:

Equation 2-7

$$V_{IN} = 2k_x \left( \frac{d_{ae}}{d_p} \right)$$

Where  $k_x$  is the angular distribution parameter,  $d_p$  represents the mean diameter of the elongated particle.

Impaction, Brownian diffusion, and sedimentation have a relationship with particle aerodynamic diameter. While electrostatic deposition has a relationship with particle charge which depends on several factors including drug formulation and material used in the devices [40].

## **2.2. Inhalation Devices**

As it was discussed in chapter 1-1, Using inhalation treatment for respiratory disease is commonly used since it delivers the drug directly into the respiratory system. Several devices have been invented for drug delivery, such as a pMDI, Nebulizer, and

DPI. The drug delivery methods, their properties, and the advantages and limitations of these devices will be discussed.

### **2.2.1. Pressurized Metered-Dose Inhaler(pMDI)**

George Maison invented pMDI in the 1950s, and this device was commercialized in 1956 [41]. A pMDI (Figure 2-6) is made of a canister, actuator, formulation, metering valve, and pMDI cap. The canister is filled with a formulation, which consists of the active substance (drug), propellant system, and surfactant [42][43]. Surfactant is a substance that reduces the surface tension between propellant and drug and increases spray spreading. The pMDI delivers the drug to the lung in aerosol form. The aerosol is a pressurized or liquidized gas containing solid or liquid microparticles (metal, glass, plastic). When the formulation is injected into the air, the injected liquid is divided into smaller droplets [43]. This adiabatic process is called *primary breakup (flash breakup)*, and the pressure difference between the canister (300-500kPa [44]) and atmosphere (100kPa) is the main reason for the primary breakup. During the secondary break-up, droplets are divided into even smaller sizes. Secondary breakup occurs in five modes which are explained in page 28.

The particle distribution and size are influenced by several parameters[45]. The parameters pertaining to the distribution of the particles comprise the internal coating of the container, propellant pressure, the mixture type, the formulation (drug concentration and particle size, ethanol percentage), metering valve design, the waiting time between actuation and inhalation, nozzle diameter, spray velocity and the inhalation coordination with actuation. Regarding particle size parameters, formulation of medicine, primary atomization, and secondary particle break up are three factors that have a direct relation with particle size [45].

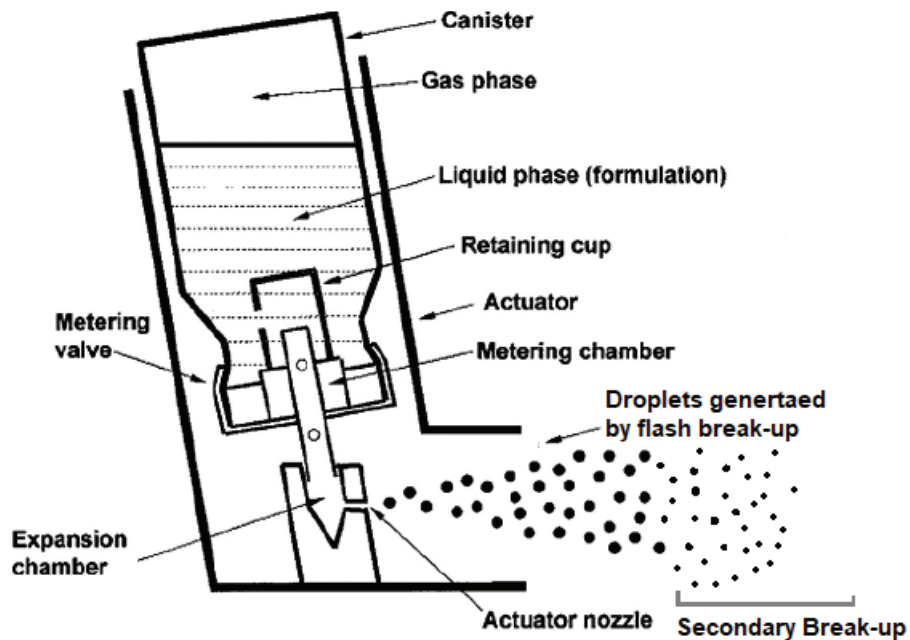


Figure 2-6 Schematic of pressurized metered-dose inhaler[46]

The earlier pMDI propellant was Chlorofluorocarbons (CFC). The CFC comprises chlorine, fluorine, carbon, and possibly hydrogen [47]. On 26 August 1987, the Montreal Protocol on Substances that Deplete the Ozone Layer was signed between countries to limit the production of the greenhouse gases [47]. Accordingly, the CFC propellant was needed to be replaced by other gases. The hydrofluoroalkanes (HFA) and tetrafluoroethane (HFA 134a) are the best candidates[47]. Some research compared the drug delivery and particle size of HFA and CFC pMDI. The total drug deposition in the lung is similar for HFA 134a and CFC. However, some changes were needed to be made in the pMDI design, since the HFA 134a and CFC have different thermodynamic properties [48]-[49]. It was observed that higher propellant proportion generates finer particles (1.1-4.7 micrometer) percentages[50], [51]. Although plume velocity is independent of propellant percentage, the effect of propellant percentage on particle size is significant [52].

The key advantages of pMDI over other inhaler devices are cost-effectiveness, pocketable size, and higher drug delivery rate [53]. On the other hand, patient inhalation coordination is needed for maximizing drug delivery with pMDI. The breath-actuated pMDI was invented to overcome this problem, but it is more expensive than regular pMDI [53]. Furthermore, the breath-actuated pMDI cannot resolve the particle deposition problem in the patient's mouth. The spacer and VHC were invented to overcome breathing coordination and drug deposition in the mouth.

## 2.2.2. Spacer and Valved Holding Chamber (VHC)

VHCs and spacers are two types of add-on devices that improve the pMDI drug delivery [54],[55]. They reduce the particle size by providing sufficient time for the secondary break up, but this relation is not linear, since the particle sedimentation increases over time. M.Nageland et al. investigated the effect of the delay on drug delivery of VHCs [56]. The no-delay, 2-second delay, and 10-second delay were observed in this study. Their result indicated that the delay decreases the VHCs drug delivery.

As explained earlier in 2.1.3 (Inertial Impaction), the high-momentum particles may not follow the patient's inhalation flow to the lung, and they may impact the patient's mouth [57]. Therefore, low-speed particles have a higher chance to deposit in the lung. Therefore, the particle deposition in the mouth decreases by using spacer/VHC since it helps to reduce particle velocity [58][59]. Moreover, Terzano et al. showed that the VHC increases the number of delivered fine particles (1.1-4.7 micrometer) [60]. They claimed that the secondary breakup may be the reason for this increase.

Another study investigated the effect of the electrostatic charge of the spacer's body in drug delivery [61]. They chose the Volumetric spacer, and they removed the surface electron charge. They claimed that the drug delivery was highest when the surface electrostatic charge was zero. Suggett et al. also compared the drug delivery of two non-conducting VHC and two antistatic VHC [62]. The result of this experiment indicates that employing anti-static VHC increases the amount of delivered fine particles.

Ricardo et al. simulated the volumetric spacer and studied the flow inside this VHC in a CFD study [63]. Then, they designed a pear-shaped spacer and studied the flow inside of it. The recirculation regions in the pear-shaped spacer were smaller than the simple volumetric spacer. The recirculation region is a stationary vortex (the rotating region around an axial) that has a reverse direction of the prevailing flow direction [64]. The pressure difference between two points in a region causes backflow which generates a recirculation zone [65]. Ricardo and his team claimed that the spacer shape and design influence recirculation size near the wall [63]. Since, the recirculation area traps the fine particle inside the spacer, reducing the vortex size increases the fine particle delivery. Sarkar et al. [66] also claimed there is a direct relationship between the quantity of recirculation area and drug deposition.

In another study, the authors developed a new spacer design to enhance spacer drug delivery [67]. They used Volumatic spacer as a starting point to design twelve valves and eight spacers' bodies shown in Figure 2-7. Their study can be divided into three sections. First, they compared the flow streamlines inside eight spacers and chose the best body among the eight designs. It was assumed that recirculation regions reduce the spacer's delivery. Therefore, the design with less recirculation area was chosen as the best body design. Body number six showed minimum recirculation regions among other spacers. Then, the authors simulated the airflow near all twelve-valve designs and observed the recirculation near valves. The valve design number 9 produced less recirculation region. In the last stage of the study, they combined the best valve design (design number 9) with the best body geometry (design number 6). The study claimed that this combination improved the drug delivery of the VHC since the recirculation area was reduced.

The drug delivery of two market-available VHCs was investigated with the experimental and numerical method to reveal the particle deposition pattern inside the spacers [68]. Each spacer was divided into four regions: upper and lower front section, upper and lower back section. The result indicated that the drug deposition in the lower half of the spacer is greater than in other regions in both VHCs. The spray angle was known as a reason for this asymmetric deposition. Moreover, the result illustrated that the inhalation flow rate affected the location and amount of particle deposition on the spacer wall. They suggested an asymmetric spacer design to improve the spacer drug delivery.

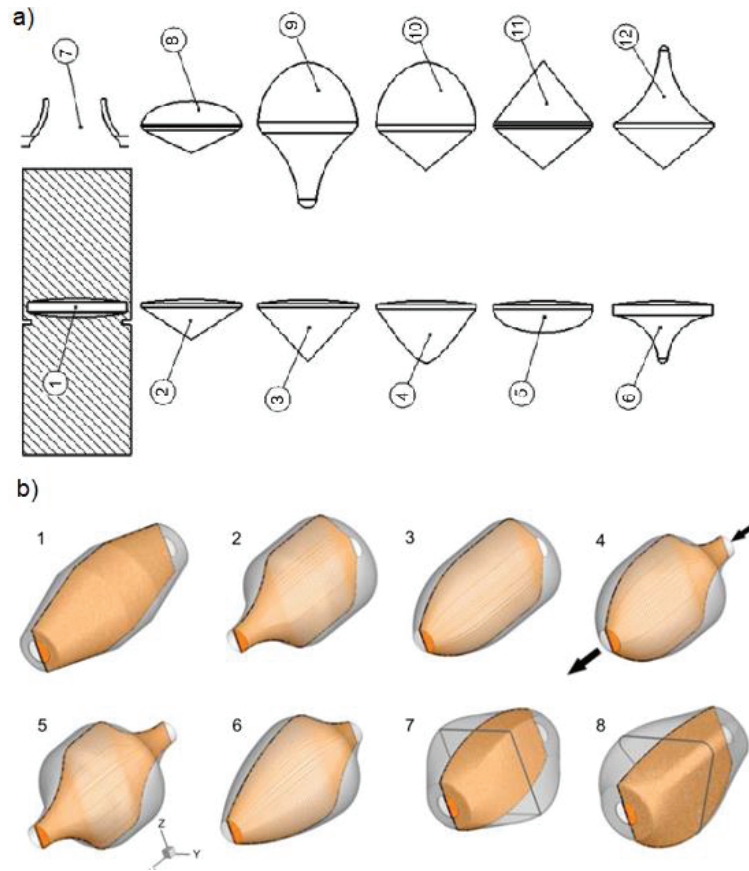


Figure 2-7 Ricardo's study a) twelve configurations of valve b) eight configurations of body design [67]

In conclusion, studies showed that the spacer/VHC can improve the delivered dose to the patient's lung[54]-[55]. The drug delivery of spacers depends on electrostatic charge[62], spacer design[69], valve design[67], breathing patterns, inhalation flow [60], and spacer size [70]–[73], [74].

### 2.2.3. Nebulizer

Nebulizer is a device that continuously transfers the liquid into aerosol and the patient's inhalation delivers the generated aerosol to the lung directly [53]. In effect, the inhalable particles pass through the mouthpiece and deliver to the lung while the coarse particles ( $>10 \mu m$ ) stay in the nebulizer and return to the liquid reservoir then it will be re-atomized later [75]. Nebulizers are categorized based on methods used for converting the liquid into respirable particles. The methods are including pneumatic (jet and

hydrodynamic), electric(ultrasonic)[18], and vibrating-mesh nebulizers[76]. Figure 2-8 shows three types of nebulizers. The particle size and drug delivery of nebulizers depend on its type and properties of the fluid [77].

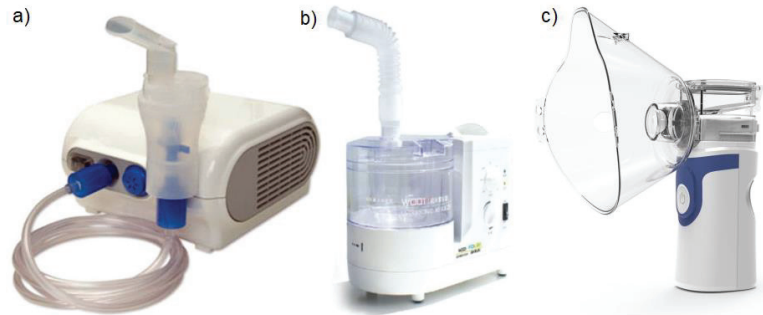


Figure 2-8 a) Jet Nebulizer b) Ultrasonic Nebulizer c) Vibrating-Mesh nebulizer

Jet nebulizer converts liquid to small droplets by passing high-velocity gas through a narrow orifice [78]. Jet nebulizer has several types like breath enhance jet nebulizer or breath-actuated jet nebulizers. The amount of delivered aerosol from the nebulized mouthpiece increases during inhalation. Breath actuated jet nebulizer is activated by patient inhalation [78].

Ultrasonic nebulizer uses ultrasonic energy to produce aerosol [75]. The piezoelectric inside the nebulizer produces vibration (1-3 MHz) that passes through the liquid medicine and produces the aerosol. The particle size has a direct relation with the vibration frequency [78]. Ultrasonic nebulizer produces heat during producing an aerosol that can break down drug protein[76].

Mesh nebulizer is a new generation of nebulizer that produces fine aerosol particles in a silent operation [79]. In this device, the drug formulation (liquid) passes through a mesh which is vibrated by piezoelectrics (Figure 2-9). The high-frequency piezoelectric vibration (about 1.8kHz) pushes the liquid into the mesh plate that has thousands of holes with  $3\mu\text{m}$  diameters [80]. As a result, the device generates the mist of drug fine particles ( $1.1\text{-}4.7\mu\text{m}$ ) with minimum drug waste in comparison with other nebulizers.



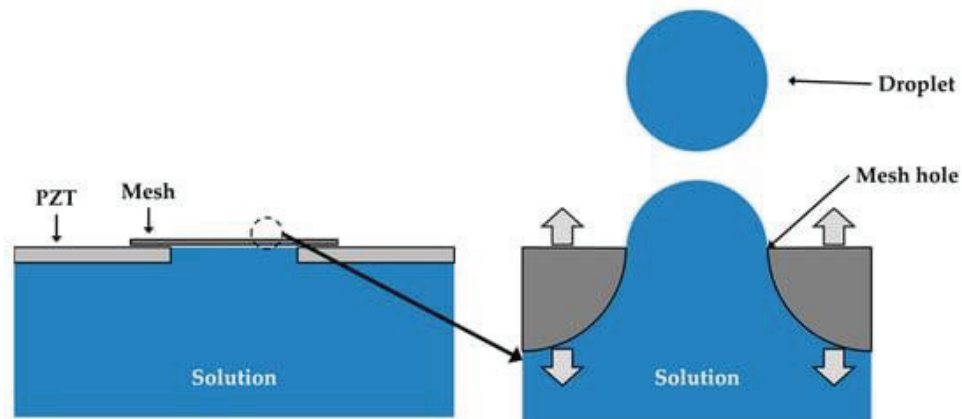


Figure 2-9 Vibrating mesh nebulizer mechanism schematic[79].

Overall, The drug delivery of the mesh nebulizer is the highest than jet nebulizer and ultrasonic nebulizer [49]. Moreover, the mesh nebulizer is pocket-size, has a short treatment time, and has a high percentage of fine particles. However, complicated cleaning techniques and high prices are two main drawbacks of the Vibrating-mesh nebulizer [76]. On the other hand, an ultrasonic nebulizer and a jet nebulizer are spacious with long treatment times that make them inconvenient for daily usage.

#### 2.2.4. Dry Powder Inhaler

Dry powder inhaler (DPI) is a non-propellant base inhaler that delivers the drug to the lung in a solid formulation [81]. The micronized drug particles ( $1-5\mu m$ ) attach on the surface of coarse carrier particles which facilitate the drug flow to the lung [80]. The aim of carrier particles is to deliver the drug particles to the lung and then the drug particles detach from carrier particles surface during inhalation. However, sometimes inhalation flow does not have sufficient energy to overcome the adhesion forces between the drug and the carrier particle [82]. Therefore, the attached drug particles and the carrier which have a large aerodynamic diameter ( $> 50\mu m$ ) deposit on patient mouth by impaction mechanism [80]. It was observed that the carrier's physical-chemical properties have a direct relationship with particle deposition patterns [80].

DPI is categorized into two groups: passive and active [83]. In the active DPI, electrical or mechanical energy is provided by the device to facilitate the particle break up. However, in a passive dry powder inhaler, the flow produced by the patient is the only source of energy for particle break up. Although active DPI generates a higher percentage of fine particles than passive DPI, its cost is the main drawback that impedes widespread usage [83].

## 2.3. Conclusion

By comparing the advantages and limitations of each inhalation device, it can be concluded that pMDI has key advantages over nebulizers and DPI. In terms of particle breakup, pMDI dependency on inhalation flow rate is lower than DPI. In fact, passive DPI rely only on patient flow for drug detachment from carrier particles, so the patient should inhale deep with a high flow rate to receive the prescribed dosage [83]. Therefore, passive DPI is not an appropriate treatment option for children, seniors, and adults who cannot produce a high flow rate of breath. Moreover, DPI dependency on the patient causes uninformed delivered dosage [84], while pMDI+ VHC delivers repeatable dosing in every puff [42].

Although a nebulizer requires less inhalation coordination and delivers a higher fraction of fine particles in comparison with pMDI [82], it is more expensive than the pMDI and DPI. Furthermore, the large size of the jet nebulizer and ultrasonic nebulizer and their dependency on external sources of energy make it inconvenient for daily use. On the other hand, pMDI provides a shorter treatment time than nebulizers which makes it convenient.

However, pMDI has some limitations including requiring precise inhalation coordination with pMDI actuation and depositing particles in the mouth. These can be addressed by using a spacer/VHC. It was shown that pMDI drug delivery improves by using a spacer/VHC [54], [55], [60], and drug deposition in a patient's mouth significantly decreases [58][59]. However, it was observed that the spacer design has an effect on delivered particles' size and amount [67], [70]–[73]. Some claimed that the recirculation zone is the reason for VHCs performance difference [63]–[67]. Therefore, this thesis contributes to 1) identifying the effect of flow streamlines and recirculation zone in particle delivery; 2) optimizing the spacer design for increasing delivered fine particles for higher lung absorption.

## **Chapter 3.**

### **Numerical Study**

#### **3.1. Introduction**

Computational Fluid Dynamics (CFD) solves fluid equations by employing the discretization method in computer simulation [85]. R. Courant et.al solved the first two-dimension CFD modeling in 1928 and then CFD was developed for three-dimension modeling [86],[87]. Nowadays, CFD has a crucial role in aerospace, ship design, tool design, automobile and engine applications, civil engineering, and environmental engineering.

In this chapter, the role of secondary inlets and static blades are explored using a CFD study. PARI VORTEX VHC was modeled, and the flow inside of the spacer was simulated in two conditions including the secondary inlets were open or close.

#### **3.2. Material and Method**

To set up a CFD study for simulating the flow insider of the spacer, initially, the PARI VORTEX geometry is modeled in ANSYS Space Claim. Then a mesh convergence study is set out to examine that the simulation outcomes are not affected by the size of the grids. Next, to model drug particles in ANSYS, it is required to define the particle distribution model and secondary breakup method. Therefore, in this chapter, two different distribution mathematical models and five secondary breakup models are explained. Then, Navier-Stokes equations, which are a mathematical model to predict flow behavior, are discussed, and three famous turbulence models are explained and compared. As a result, this CFD study selects the turbulence model with the highest advantages. Later, to simulate flow inside the spacer, the boundary conditions are defined. Finally, the CFD result of open secondary inlets spacer (OSIS) and close secondary inlets spacer (CSIS) are compared.

### 3.2.1. Geometry and Mesh

The geometry of the VORTEX VHC and a partial pMDI are modeled in Space Claim software (Figure 3-1). A calibrated Mitutoyo Caliper is employed to measure the PARI VORTEX dimension at 20 centigrade room temperature. VORTEX's total length is 141.5mm with the largest diameter of 48mm. The total length of the valve is 21mm with an assumption that the open valve has an ellipse cross-section at the end of 3.3mmX17.3mm. A pMDI injection location is modeled with a circle with 0.25mm diameter [66]. PARI latest VORTEX design has a feature to avoid exhaling inside the VHC. This part of the spacer is not modeled in Space Claim, since this CFD study focuses on the flow behavior during inhalation.

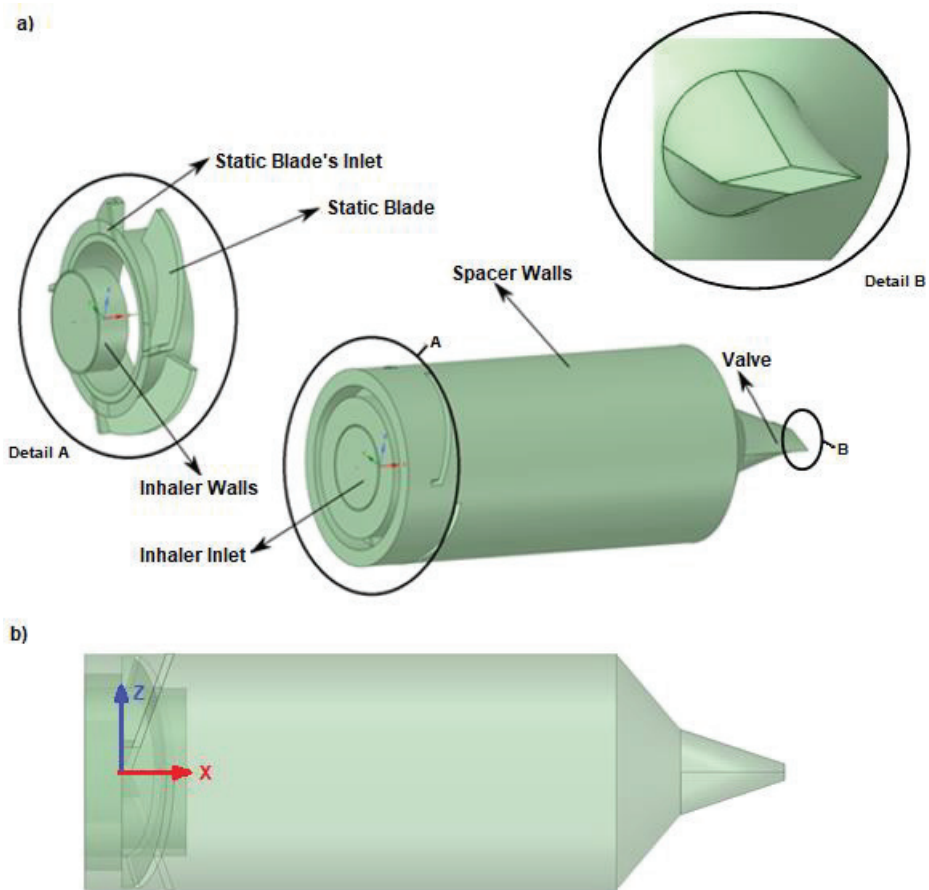
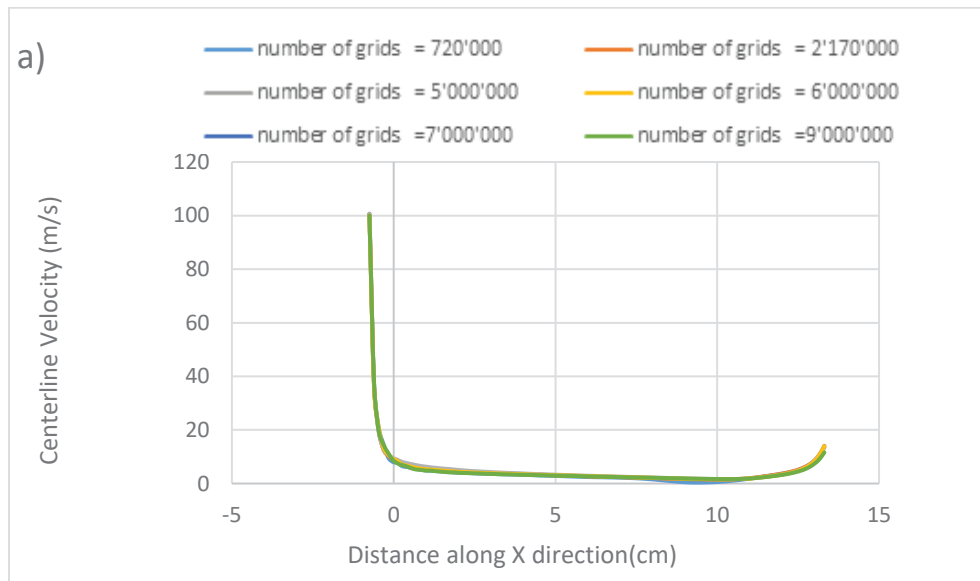


Figure 3-1 a) VORTEX schematic and boundaries locations b) Coordination position in VORTEX

Grids are generated with ANSYS Meshing where some modifications are applied to increase the mesh quality. Mesh quality is measured with the skewness factor in this

thesis. The ideal mesh element's edges are equal, and the skewness factor is calculated based on the difference between grids' shape with the ideal grid [88]. Mesh with average skewness less than 0.33 and the maximum skewness smaller than 0.95 is acceptable for the CFD study [88]. Even though the mesh quality is acceptable, a mesh convergence study is needed for examining the CFD result is not affected by the number of grids. Therefore, several grid sizes are chosen including 720'000, 2'170'000, 5'000'000, 6'000'000, 7'000'000, and 9'000'000 grids for the mesh convergence study. Steady-state simulation is established with a constant flow rate of 28.3L/min at the outlet and the 1000 particles of salbutamol injected into the VHC with 80m/s velocity for all these six grids' sizes [89][90]. The spacer centerline velocity, the velocity along with y and z inlet axils are compared in a mesh study [89][90]. The result has been shown in Figure 3-2. The centerline velocity for all mesh numbers is thoroughly overlapped which represents grid sizes do not affect the centerline velocity (Figure 3-2-a). By comparing Figure 3-2-b and Figure 3-2-c, it can be concluded that the difference between 9'000'000 and 7'000'000 is negligible. The grid sizes are not fine enough to capture the inlet Velocity along z-direction (Figure 3-2-c) in 1720'000, 2'170'000, 5'000'000, and 6'000'000 as accurate as 7 million and 9 million meshes. Therefore, 7'000'000 mesh is used in the rest of the simulations. Its average skewness is 0.26825 and 0.81 maximum skewness factor.



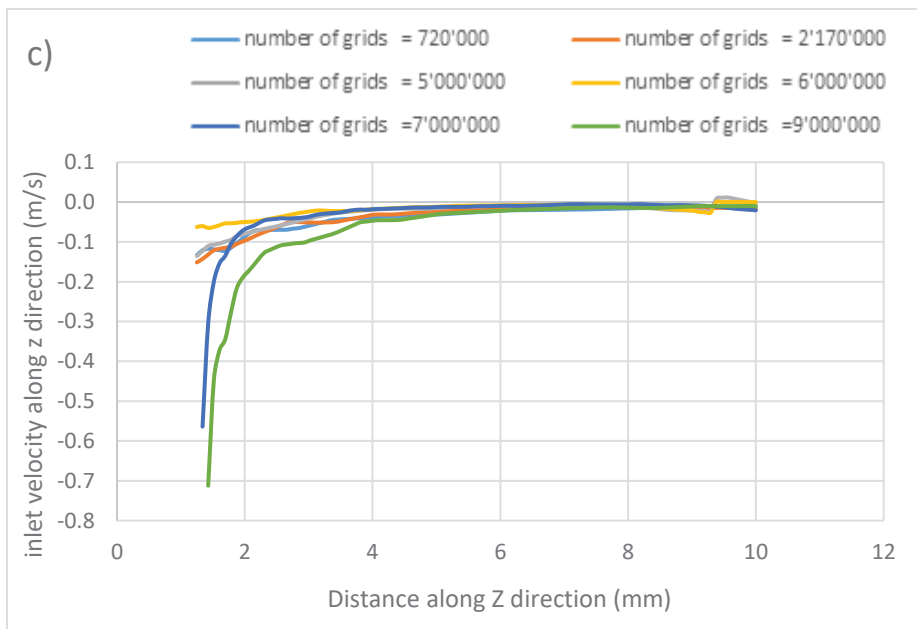
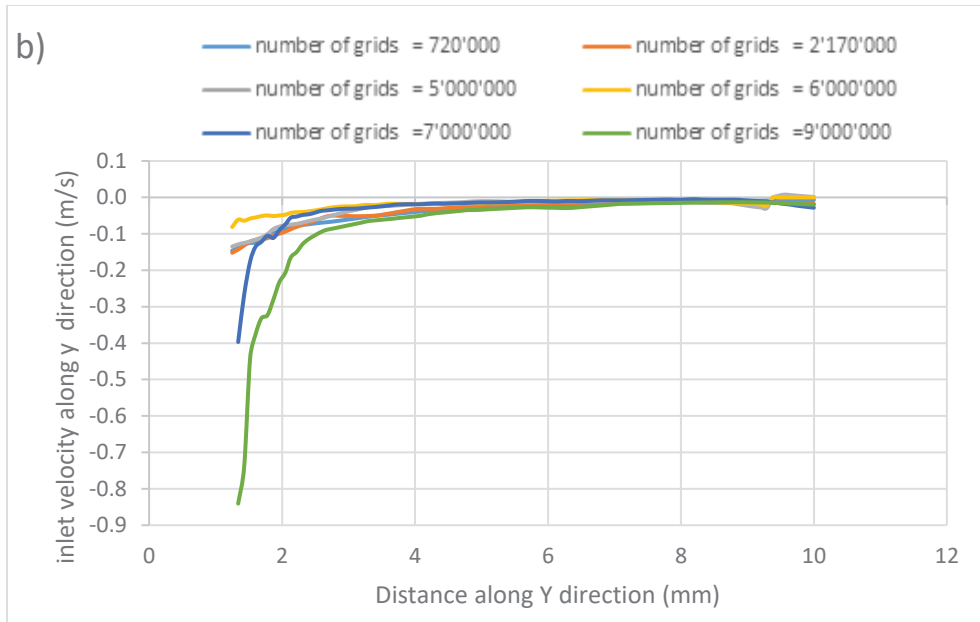


Figure 3-2 Comparisons of flow velocity a) centerline velocity of the spacer b) velocity along y-direction in inlet surface b) velocity along z-direction in inlet surface

### 3.2.2. Particle Modeling

#### ***Particle Tracking Modeling***

Lagrangian Particle Tracking is used to simulate dispersed multiphase[91]. In this method, every single particle is tracked from the injection point to the outlet, and then the average of the particle behavior is reported as the result [87][92][91]. The Lagrangian particle tracking method provides complete information about particle behavior, and it uses the force balance on a particle which can be written as [93]:

Equation 3-1

$$\frac{du_p}{dt} = F_D + F_G + F_B$$

The right side of the equation represents drag force ( $F_D$ ), gravity force ( $F_G$ ), buoyancy force ( $F_B$ ) on the particle. The  $u_a$  is ambient flow velocity,  $u_p$  is particle velocity,  $\rho_a$  is ambient flow density and the  $\rho_p$  is particle density. The drag force equals [80]:

Equation 3-2

$$F_D = \frac{1}{2} C_D \rho_a A_a |u_a - u_p| (u_a - u_p)$$

Where the  $C_D$  is the drag coefficient and  $A_a$  represents deformed particle cross-section. The Reynolds number ( $Re$ ) and the drag coefficient are defined in Equation 3-3 and Equation 3-4, respectively:

Equation 3-3

$$Re = \frac{\rho_a D_p |u_p - u_a|}{\mu}$$

Equation 3-4

$$C_D = a_1 + \frac{a_2}{Re} + \frac{a_3}{Re^2}$$

In Equation 3-4,  $a_1$ ,  $a_2$  and  $a_3$  are constants.

Gravity and buoyancy forces are [93]:

Equation 3-5:

$$F_B + F_G = \frac{(\rho_P - \rho_a)\pi d_p^3}{6} g$$

Where  $d_p$  is particle diameter.

### **Particle Breakup**

Particle atomization occurs in two stages including primary break up and secondary break up. Primary breakup happens due to the pressure difference between inhaler canister and ambient pressure. This process occurs very fast that the process is considered as adiabatic since there is not enough time for heat transfer[94]. In this study, drug particles are assumed solid [42], therefore the primary breakup is not modeled in this CFD study [95]. The secondary break up which occurs due to rapid acceleration, high shear stresses, and turbulent fluctuations [96] can occur in five modes in Newtonian fluid [97] that are including Vibrational breakup, Bag breakup, Bag and Stamen breakup, sheet striping, and Catastrophic breakup (Figure 3-3).

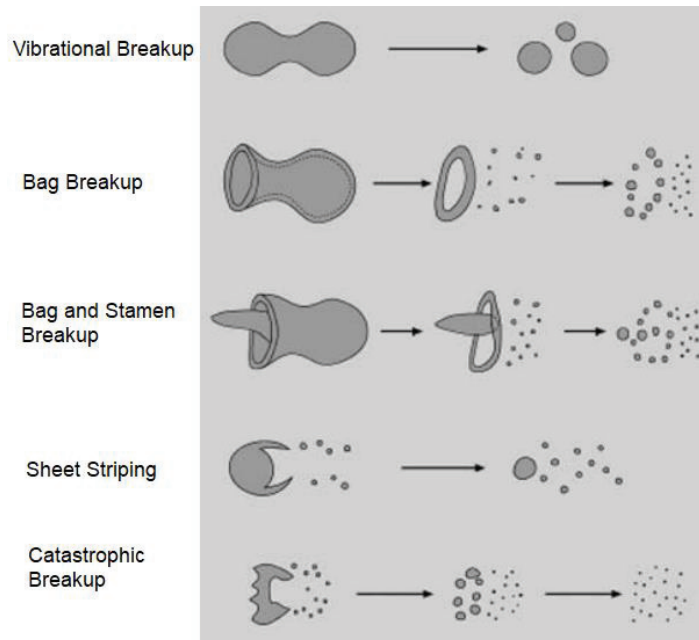


Figure 3-3 Newtonian Particle Breakup Modes [97]

The first mode in a secondary breakup is vibrational breakup where Newtonian particle natural frequency divides the droplet into smaller particles [97]. Bag breakup



occurs when a particle is defragmented into a ring-shaped droplet and smaller droplets, later that ring shaped particle also breakup into smaller particles. In Bag and Stamen breakup first, the droplet is defragmented into a stamen, a ring-shaped droplet and smaller droplets. Later, the ring-shaped droplets and the stamen, which is parallel to parallel to particle velocity direction, break up into smaller size droplets. Another mode for secondary particle breakup is Sheet Striping where the particle's edge breakup happens before the center of the particle [98]. Catastrophic breakup happens when the ambient fluid defragments a particle to smaller droplets. All five Newtonian particle's Breakup modes have a relationship with a non-dimensional number which represents a ratio between the ambient flow aerodynamic force to surface tension force. This non-dimensional parameter is Weber number ( $We$ ) (Equation 3-6), and it has a direct relationship with the particle tendency to breakup [97];

Equation 3-6

$$We = \frac{\rho_a u_r^2 d_0}{\sigma}$$

$d_0$  is drop initial spherical diameter,  $\sigma$  is interfacial surface tension, and  $u_r$  is the relative velocity between particle and ambient flow. However, the effect of particle viscosity ( $\mu_p$ ) is not included in the Weber number which explains the demand for defining a new parameter [99]. To address this issue, the Ohnesorge Number ( $Oh$ ) includes the effect of viscosity in particle breakup which are defined by Equation 3-7:

Equation 3-7

$$Oh = \frac{\mu_p}{\sqrt{d_0 \rho_p \sigma}}$$

Ohnesorge Number represents the ratio of the particle viscous force to surface tension force. If the Ohnesorge Number is small ( $Oh < 0.1$ ), it can be neglected and only the Weber number is considered as a factor to quantify particle breakup tendency[98]. The relationship between Weber number and particle breakup modes for low Ohnesorge Number ( $Oh < 0.1$ ) is shown in Table 3-1.

Table 3-1 Breakup mode and Weber number range relation for  $Oh < 0.1$  [99]

Break Up mode	Weber number range
Vibrational breakup	$We < 12$
Bag breakup	$12 < We < 50$
Bag-and-stamen breakup	$50 < We < 100$
Sheet stripping	$100 < We < 350$
Catastrophic breakup	$350 < We$

ANSYS CFX provides five methods for modeling the secondary particle breakup including Reitz & Diwakar, Taylor Analogy Breakup (TAB), Enhanced Taylor Analogy Breakup (ETAB), Cascade Atomization Breakup (CAB), and Schmehl model. Reitz & Diwakar only models Bag and Stripping breakup which makes it less realistic to model pMDI particle breakup. TAB and ETAB are the two most common models for describing the inhaler particle breakup [100] [101] that use a simple spring-mass system to model force on particles. Droplet viscosity is assumed as a damping force and the surface tension performs restoring force role in this spring-mass model [99]. The only difference between TAB and ETAB is that ETAB uses a different relation to predict the particle breakup which causes the different rate of deformations and generated droplets' sizes [102]. CAB model is the enhanced version of ETAB model; however, it uses different constant values in its equation. Schmehl Breakup Model relies on experimental results to predict particle breakup which is suitable for all Ohnesorge Number values [99].

The critical Weber number ( $We_{crit}$ ) from which the breakup starts is calculated by Equation 3-8:

Equation 3-8

$$We_{crit} = 12(1 + 1.0770h^{1.6})$$

Particle breakup only occurs if the Weber number is larger than the critical Weber number. The relation between particle breakup mode and Weber number in Schmehl Model is shown in Table 3-2 :

Table 3-2 Breakup regime for Schmehl Breakup Model [102]

Breakup Regime	Weber number range	Child droplet radius
Bag Breakup	$12(1 + 1.0770h^{1.6}) < We$ $< 20(1 + 1.20h^{1.5})$	$d_{32} = d_p(1.50h^{0.2} \left( \frac{We}{1 + 1.0770h^{1.6}} \right)^{-0.25})$
Bag-and-stamen breakup	$20(1 + 1.20h^{1.5}) < We$ $< 32(1 + 1.50h^{1.4})$	$d_{32} = d_p(1.50h^{0.2} \left( \frac{We}{1 + 1.0770h^{1.6}} \right)^{-0.25})$
Shear Breakup	$32(1 + 1.50h^{1.4}) < We$	$d_{32,red} = \frac{4d_{32} \left( \frac{We_{crit}\sigma}{\rho_F V_{slip}^2} \right)}{5 \frac{We_{crit}\sigma}{\rho_F V_{slip}^2} - d_{32}}$

In this simulation, the Schmehl Breakup model is chosen to predict inhaler droplets in secondary atomization and generated particles' aerodynamic diameter, since it is based on experimental findings, we found it more realistic to model pMDI particle breakup.

### **Particle Distribution**

pMDI produces aerosol which consists of particles of different sizes[83]. The aerosol distribution can be modeled by mathematical models, and the two most commonly used mathematical distribution models are Log-Normal and Rosin Rammler [42].

### **Log-Normal**

The Log-Normal distribution is defined as follow:

Equation 3-9

$$f(d_p; \mu, \sigma) = \frac{1}{d_p \sigma \sqrt{2\pi}} e^{-\frac{1}{2} \left( \frac{\ln d_p - \mu}{\sigma} \right)^2}$$

Where  $\mu$  and  $\sigma$  represent the natural logarithm of the mean particle diameter and standard deviation, respectively. The standard deviation of the Log-Normal can be calculated by using Equation 3-10 [103][42].

Equation 3-10

$$\sigma = \left( \frac{d_{84}}{d_{16}} \right)^{\frac{1}{2}}$$

Where  $d_{16}$  is a diameter that is smaller than 16% of the particles, and  $d_{84}$  is a diameter that is smaller than 84% of the particles.

### **Rosin Rammler**

The Rosin Rammler is another popular mathematical model to describe aerosol particle distribution[100]. The mass fraction(R) can be calculated by using Equation 3-11:

Equation 3-11

$$R = \exp \left[ - \left( \frac{d}{d_e} \right)^k \right]$$

In Equation 3-11,  $d_e$  and  $k$  are mean diameter and spread parameters, respectively.  $d_e$  and  $k$  are two variable parameters that help to fit the mathematical model to experimental data. Reduction in the spread parameter causes a wider shape of the distribution model, and the reduction in mean diameter moves the diagram to the left side toward the smaller size particles [104].

Ricardo et al. compared three mathematical models with experimental data. They concluded that the Rosin Rammler mathematical model showed a good agreement with experimental findings. Furthermore, other studies used the Rosin Rammler model with different parameters (Table 3-3) to simulate pMDI aerosol distribution [42], [66], [68].

Table 3-3 Rosin Rammler Parameters

Team	Mean Diameter ( $\mu\text{m}$ )	Spread Parameter	Size Range ( $\mu\text{m}$ )
Ricardo[42]	16.54	1.86	1.22-49.5
Sarkar [66]	2.65	1.5	1-10
Ogrodnik [68]	12.2	1.44	-

### ***Spray Simulation***

This thesis uses Ventolin medication in pMDI for CFD simulation and experiment, which is widely used to study pMDI and VHC performance in experimental and numerical studies [16], [73], [105]. Ventolin HFA consists of salbutamol and HFA-134a propellant [42]. Since the propellant particle evaporation occurs quickly [42], [66], [68], evaporation is not considered in this simulation. Therefore, salbutamol particles are considered the only particles fired into the spacer. In this thesis, 1000 salbutamol particles are injected with 100m/s velocity and 0.001[g/s] mass flow rate uniformly from the injection surface boundary. The Rosin Rammler distribution with 1.315 Spread Parameter and 3.75 [ $\mu\text{m}$ ] Mean diameter is chosen to model particles distribution. The drug characteristic is shown in Table 3-4.

Table 3-4 Drug Characteristic

Properties	Value
Density [ $\text{Kg}/\text{m}^3$ ]	1230
Actuation dose [ $\mu\text{g}$ ]	100
Salbutamol mass flow rate [Kg/s]	1.0e-6
Particle breakup	Schmehl Breakup Model
Number of particles	1000
Particle Position	Random Uniform injection
Particle Distribution	Rosin Rammler

### **3.2.3. Flow Modeling and Boundary Condition**

#### ***Navier–Stokes Equations and Turbulence Model***

Navier–Stokes equations define the Newtonian flow behavior which use the conservation of mass, the conservation of momentum (Newton's second law), and the conservation of energy laws (the first law of Thermodynamics) [106]:

Equation 3-12: conservation of mass

$$\frac{\partial \rho}{\partial t} + \nabla \cdot (\rho \vec{V}) = 0$$

Equation 3-13: x-direction Momentum

$$\rho \frac{Du}{Dt} = -\frac{\partial P}{\partial x} + \mu \left[ \frac{\partial^2 u}{\partial x^2} + \frac{\partial^2 u}{\partial y^2} + \frac{\partial^2 u}{\partial z^2} \right] + \rho f_x$$

Equation 3-14: y-direction Momentum

$$\rho \frac{Dv}{Dt} = -\frac{\partial P}{\partial y} + \mu \left[ \frac{\partial^2 v}{\partial x^2} + \frac{\partial^2 v}{\partial y^2} + \frac{\partial^2 v}{\partial z^2} \right] + \rho f_y$$

Equation 3-15: z-direction Momentum

$$\rho \frac{Dw}{Dt} = -\frac{\partial P}{\partial z} + \mu \left[ \frac{\partial^2 w}{\partial x^2} + \frac{\partial^2 w}{\partial y^2} + \frac{\partial^2 w}{\partial z^2} \right] + \rho f_z$$

Equation 3-16: Energy Equation

$$\begin{aligned} & \frac{\partial}{\partial t} \left[ \rho \left( e + \frac{u^2 + v^2 + w^2}{2} \right) \right] \\ &= \rho \dot{q} + \frac{\partial}{\partial x} \left( k \frac{\partial T}{\partial x} \right) + \frac{\partial}{\partial y} \left( k \frac{\partial T}{\partial y} \right) + \frac{\partial}{\partial z} \left( k \frac{\partial T}{\partial z} \right) - \frac{\partial(uP)}{\partial x} - \frac{\partial(vP)}{\partial y} - \frac{\partial(wP)}{\partial z} \\ &+ \frac{\partial(u\tau_{xx})}{\partial x} + \frac{\partial(u\tau_{yx})}{\partial y} + \frac{\partial(u\tau_{zx})}{\partial z} + \frac{\partial(v\tau_{xy})}{\partial x} + \frac{\partial(v\tau_{yy})}{\partial y} + \frac{\partial(v\tau_{zy})}{\partial z} + \frac{\partial(w\tau_{xz})}{\partial x} \\ &+ \frac{\partial(w\tau_{yz})}{\partial y} + \frac{\partial(w\tau_{zz})}{\partial z} + \rho \vec{f} \cdot \vec{V} \end{aligned}$$

Where  $u$ ,  $v$  and  $w$  are the velocity of flow along the x, y, and z-axis, respectively.  $f_x$ ,  $f_y$ , and  $f_z$  represent external force along x, y, and z-direction respectively. The pressure of the flow and flow density are symbolized as  $P$  and  $\rho$ .  $\tau$  is viscous stresses and  $k$  is thermal conductivity.  $\dot{q}$  represents heat transfer rate.  $T$  and  $t$  are temperature and time, respectively.

Solving Navier–Stokes equations is relatively complex for turbulent flow, therefore, turbulence models are employed to calculate the effect of turbulence in flow [107]. Turbulence models include Reynolds Averaged Navier-Stokes equations (RANS), Large

Eddy Viscosity (LES), and Direct Numerical Simulation (DNS). Since LES and DNS computational costs are expensive [108], therefore three well-known RANS models are discussed in this thesis.

### Reynolds Averaged Navier-Stokes (RANS)

RANS models can be categorized by the number of additional equations that they add to Navier-Stokes equations including zero-, one-, and two-equations [91]. Two-Equations RANS turbulence models were used in different spacer and pMDI simulation studies; therefore, this thesis focuses on popular Two-Equations RANS [63], [66], [100], [109], [110].  $k - \varepsilon$ ,  $k - \omega$ , and Shear stress transport (SST) are three popular two-Equations RANS that were used to solve turbulent Navier-Stokes equation in pMDI simulations [63], [66], [100], [109], [110].

#### RANS Two-Equations Models

$k - \varepsilon$  is one of the well-known RANS two equations model, where  $k$  refers to turbulent kinetic energy and  $\varepsilon$  represents turbulence eddy dissipation. Therefore, the continuity equation and momentum equation are:

Equation 3-17

$$\frac{\partial \rho}{\partial t} + \frac{\partial}{\partial y}(\rho v) = 0$$

$$\frac{\partial \rho u_i}{\partial t} + \frac{\partial}{\partial y}(\rho uv) = -\frac{\partial p'}{\partial t} + \frac{\partial}{\partial y} \left( \mu_{eff} \left( \frac{\partial u}{\partial y} + \frac{\partial v}{\partial x} \right) \right) + S_M$$

Where  $p'$ ,  $\mu_{eff}$ ,  $S_M$  are modified pressure, effective viscosity accounting for turbulence, and the sum of body forces, respectively. The effective viscosity equation is then:

Equation 3-18

$$\mu_{eff} = \mu + \mu_t$$

The turbulence viscosity is:

Equation 3-19

$$\mu_t = C_\mu \rho \frac{k^2}{\varepsilon}$$

The value of  $k$  and  $\varepsilon$  are calculated from below two-equations:

Equation 3-20

$$\frac{\partial(\rho k)}{\partial t} + \frac{\partial}{\partial j}(\rho v k) = \frac{\partial}{\partial y} \left[ \left( \mu + \frac{\mu_t}{\sigma_k} \right) \frac{\partial k}{\partial y} \right] + P_k - \rho \varepsilon + P_{kb}$$

$$\frac{\partial(\rho \varepsilon)}{\partial t} + \frac{\partial}{\partial y}(\rho v \varepsilon) = \frac{\partial}{\partial y} \left[ \left( \mu + \frac{\mu_t}{\sigma_\varepsilon} \right) \frac{\partial \varepsilon}{\partial y} \right] + \frac{\varepsilon}{k} (C_{\varepsilon 1} P_k - C_{\varepsilon 2} \rho \varepsilon + C_{\varepsilon 1} P_{\varepsilon b})$$

Where  $C_\mu$ ,  $C_{\varepsilon 1}$ ,  $C_{\varepsilon 2}$ ,  $\sigma_k$  and  $\sigma_\varepsilon$  are constants.  $P_k$  represents the turbulence production due to viscose forces, and it equals to[108]:

Equation 3-21

$$P_k = \mu_t \left( \frac{\partial u}{\partial y} + \frac{\partial v}{\partial x} \right) \frac{\partial u}{\partial y} - \frac{2}{3} \frac{\partial w}{\partial z} \left( 3\mu_t \frac{\partial w}{\partial z} + \rho k \right)$$

Although this model is a great option to calculate the recirculation area, it is not an accurate model for complex flow with strong streamline curvature [111][112].

$k - \omega$  is another popular two-equation RANS model where  $\omega$  represents the turbulence frequency.  $k$  and  $\omega$  can be calculated from Equation 3-22 [108]

Equation 3-22

$$\frac{\partial(\rho k)}{\partial t} + \frac{\partial}{\partial y}(\rho v k) = \frac{\partial}{\partial y} \left[ \left( \mu + \frac{\mu_t}{\sigma_k} \right) \frac{\partial k}{\partial y} \right] + P_k - \beta' \rho k \omega + P_{kb}$$

$$\frac{\partial(\rho \omega)}{\partial t} + \frac{\partial}{\partial y}(\rho v \omega) = \frac{\partial}{\partial y} \left[ \left( \mu + \frac{\mu_t}{\sigma_\omega} \right) \frac{\partial \omega}{\partial y} \right] + \alpha \frac{\omega}{k} P_k - \beta \rho \omega^2 + P_{\omega b}$$

Where  $\beta'$ ,  $\alpha$ ,  $\beta$ ,  $\sigma_k$ , and  $\sigma_\omega$  are constant. The buoyancy production,  $P_{kb}$  for full buoyancy model and Boussinesq buoyancy model are shown in Equation 3-23 and Equation 3-24 respectively.

Equation 3-23



$$P_{kb} = -\frac{\mu_t}{\rho\sigma_\rho} g_i \frac{\partial \rho}{\partial x} \quad , \sigma_\rho = 1$$

Equation 3-24

$$P_{kb} = -\frac{\mu_t}{\rho\sigma_\rho} \rho\beta g_i \frac{\partial T}{\partial x} \quad , \sigma_\rho = 0.9$$

$P_{\omega b}$  is:

Equation 3-25

$$P_{\omega b} = \frac{\omega}{k} ((\alpha + 1)C_3 \max(P_{kb}, 0) - P_{kb})$$

$k - \omega$  is a suitable model to predict the near-wall flow, but fine-mesh grids are required in this method [91]. Moreover, this method may overpredict the eddy-viscosity, and it might show some weakness in layer separation modeling [91].

Shear stress transport (SST) is a combination of the  $k - \varepsilon$  and  $k - \omega$  methods [91]. Therefore, the simulation obtains the advantages of the two methods while minimizing errors. SST method uses the blending function to model the flow. SST two equations are [113]:

Equation 3-26

$$\frac{\partial k}{\partial t} + \frac{\partial}{\partial y}(vk) = \frac{\partial}{\partial y} \left[ (v + \sigma_k v_t) \frac{\partial k}{\partial y} \right] + P_k - (0.09)\rho k\omega + P_{kb}$$

$$\frac{\partial \omega}{\partial t} + \frac{\partial}{\partial y}(v\omega) = \frac{\partial}{\partial y} \left[ (v + \sigma_\omega v_t) \frac{\partial \omega}{\partial y} \right] + \frac{\gamma}{v_t} G - \beta\omega^2 + 2(1 - F_1) \frac{\sigma_{\omega 2}}{\omega} \frac{\partial k}{\partial y} \frac{\partial \omega}{\partial y}$$

$$G = v_t \frac{\partial u}{\partial y} \left( \frac{\partial u}{\partial y} + \frac{\partial v}{\partial y} \right)$$

$$P_k = \min(G, 0.9k\omega)$$

Where,  $\sigma_k, \sigma_\omega, \beta, \gamma$  are constants and their value is a linear combination of the corresponding coefficient:

Equation 3-27

$$\Phi = F_1\Phi_1 + (1 - F_1)\Phi_2$$

The value of  $\Phi_1$  and  $\Phi_2$  are shown in Table 3-5 which are used to calculate  $\beta'$ ,  $\sigma_k$ ,  $\sigma_\omega$ ,  $\beta$ ,  $\gamma$ .

Table 3-5  $\Phi_1$  and  $\Phi_2$  value to calculate SST constants

$\Phi$	$\sigma_k$	$\sigma_\omega$	$\beta$	$\gamma$
$\Phi_1$	0.85034	0.5	0.075	0.5532
$\Phi_2$	1.0	0.85616	0.082	0.4403

$\nu$  and  $\nu_t$  are kinetic viscosity and turbulent kinetic viscosity respectively:

Equation 3-28

$$\nu = \frac{\mu}{\rho}$$

$$\nu_t = \frac{a_1 k}{\max(a_1 \omega, SF_2)}$$

$$F_1 = \tanh(\arg_1 4)$$

$$\arg_1 = \min\left(\max\left(\frac{\sqrt{k}}{\beta' \omega y}, \frac{500\nu}{y^2 \omega}\right), \frac{4\rho k}{CD_{k\omega} \sigma_{\omega 2} y^2}\right)$$

$$CD_{k\omega} = \max\left(2\rho \frac{1}{\sigma_{\omega 2} \omega} \frac{\partial k}{\partial y} \frac{\partial \omega}{\partial y}, 1.0 \times 10^{-10}\right)$$

$$F_2 = \tanh(\arg_2 2)$$

$$\arg_2 = \max\left(\frac{\sqrt{k}}{\beta' \omega y}, \frac{500\nu}{y^2 \omega}\right)$$

Where  $y$  represents the distance from the wall. The blending function helps SST to overcome eddy-viscosity overprediction. SST method models the flow near walls using  $k - \omega$  and predict the far-field using  $k - \varepsilon$  [91]. The value of  $F_1$  is equal to one near the wall and zero in the far-field [113]. Therefore, SST method, which helps to have more

accurate flow prediction near the wall and spacer core reigns, is employed to model turbulence flow in this thesis.

### **Boundary Condition**

The steady-state simulation is set in CFX ANSYS R1 [57], [105], [114]–[116]. The airflow rate is 28 L/min at the outlet. Therefore, the mass flow rate is calculated:

Equation 3-29

$$28 \frac{L}{min} = 4.7167 \times 10^{-4} \frac{m^3}{s}$$
$$4.7167 \times 10^{-4} \frac{m^3}{s} \times 1.185 \frac{Kg}{m^3} = 5.5893 \times 10^{-4} \frac{Kg}{s}$$

The air density at 25° centigrade equals 1.185 kg/m<sup>3</sup>. The inhaler inlet is set as the opening region with 1 [atm] normal to boundary static pressure and 5% turbulence intensity. The injection face speed is set as 100 m/s where 1000 particles are injected uniformly from this surface. A non-slip wall condition is set, which means that the velocity on all wall surfaces is zero [105]. In reality, the drug's wet particles are trapped into the wall when they impact the wall; therefore, the mass flow absorption is set to 1 for all spacer walls [67]. The effect of particle impaction on airflow is negligible, and thus, the one-way coupling is set for drug and air relations. Schiller Naumann is chosen for modeling the drag force around the particles [117] which is suitable for spherical particles [99]. The turbulence numeric and advection schemes were set to a high-resolution model.

## **3.3. Result and Discussion**

In this section, the drug delivery and velocity of two OSIS and CSIS are compared. The role of secondary inlets is examined by studying the total drug delivery, mean particle diameter, and velocity contour of OSIS and CSIS.

### **3.3.1. Drug delivery**

Figure 3-4 shows the drug deposition on the spacers as well as the delivered drug at the spacers' outlet. These drugs are categorized based on their aerodynamic dimeters including Coarse Particles Percentage (CPP) (> 4.7 μm), Fine Particles Percentage (FPP)

(1.1 – 4.7 $\mu$ m), and Extra-Fine Particle Percentage (EFPP) ( $< 1.1 \mu$ m). Figure 3-4 data is calculated by:

Equation 3-30

$$\text{Spacer Deposition \%} = \left( 1 - \frac{\text{Total drug mass flow rate at outlet}}{\text{total emitted dose mass flow rate at inlet}} \right) \times 100$$

$$\text{CPP} = \frac{\text{Coarse Partcile mass flow rate at outlet}}{\text{total emitted dose mass flow rate at inlet}} \times 100$$

$$\text{FPP} = \frac{\text{Fine Partcile mass flow rate at outlet}}{\text{total emitted dose mass flow rate at inlet}} \times 100$$

$$\text{EFPP} = \frac{\text{Extra Fine Partcile mass flow rate at outlet}}{\text{total emitted dose mass flow rate at inlet}} \times 100$$

As it is shown in Figure 3-4, 30.9% of the drug is trapped inside the OSIS; and 32.9% of the emitted dose is deposited in CSIS. The trapped drug includes the deposited drug on walls and recirculation regions. In terms of CPP, OSIS delivers 0.9% less than CSIS (12.6% and 13.5%, accordingly). Based on the simulation result, FPP at OSIS and CSIS outlets equal 42% and 39.6%, respectively. Therefore, fine particle delivery is improved by more than 6% in OSIS. Moreover, delivered extra-fine parties slightly improved by using OSIS. Overall, OSIS shows better performance than CSIS by delivering a higher percentage of fine particles and reducing CPP. As explained in chapter two, coarse particles deposition on a patient mouth has side effects, and one of the motivations for using spacer is to reduce particle deposition in the mouth.

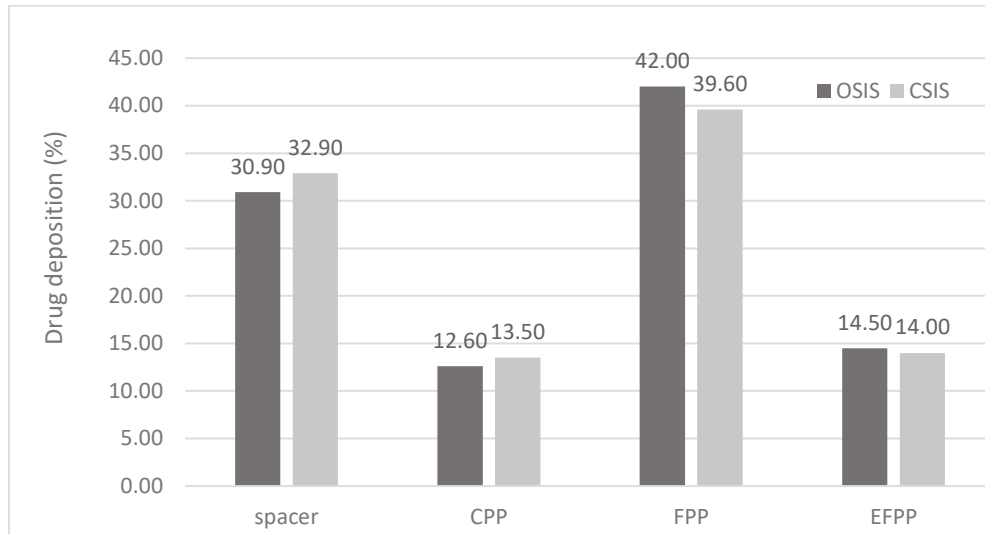


Figure 3-4 Numerical results for drug deposition in OSIS and CSIS

Table 3-6 shows CSIS and OSIS mass flow rates for six particle size groups. The first group ( $<1.1 \mu\text{m}$ ) and the last group ( $4.7\mu\text{m}<$ ) represent extra-fine particles and coarse particles, respectively. As explained in chapter 2, fine particles drug has highest chance to be absorbed by the lung, therefore in

Table 3-6 fine particles are divided into four groups to demonstrate the effect of secondary inlets in this group. Drug mass flow rates for fine particles and extra-fine particles are improved in OSIS while the coarse particle mass flow is reduced.

**Table 3-6 Salbutamol Mass Flow Rate in CSIS and OSIS**

Particle Size	CSIS-Outlet (g/s)	OSIS -Outlet (g/s)	Inlet (g/s)
$<1.1 \mu\text{m}$	1.36E-03	1.43 E-03	2.07E-03
$1.1-2 \mu\text{m}$	1.31E-03	1.33E-03	1.89E-03
$2-3 \mu\text{m}$	1.14E-03	1.26E-03	1.76E-03
$3-4 \mu\text{m}$	1.07E-03	1.12E-03	1.54E-03
$4-4.7 \mu\text{m}$	3.80E-04	4.10E-04	6.00E-04
$4.7 \mu\text{m} <$	1.51E-03	1.45E-03	2.14E-03

### 3.3.2. Velocity

The static blades change the flow streamlines which affects spacer output. One of the aims of our CFD study is to compare the velocity streamlines and contour of two spacers. Contour in ANSYS generates a plot that divides the domain into smaller regions with the same value for a given variable [118]. This feature is used to display the velocity of the domain in different locations. To capture the velocity contour in static blade inlets, two planes are defined at pMDI adaptor regions which are perpendicular to the inhaler inlet surface. Plane-1 passes through the edge of the top secondary inlet with a 24-degree angle with XY Plane, and Plane 2 is perpendicular to Plane-1 (Figure 3-5).

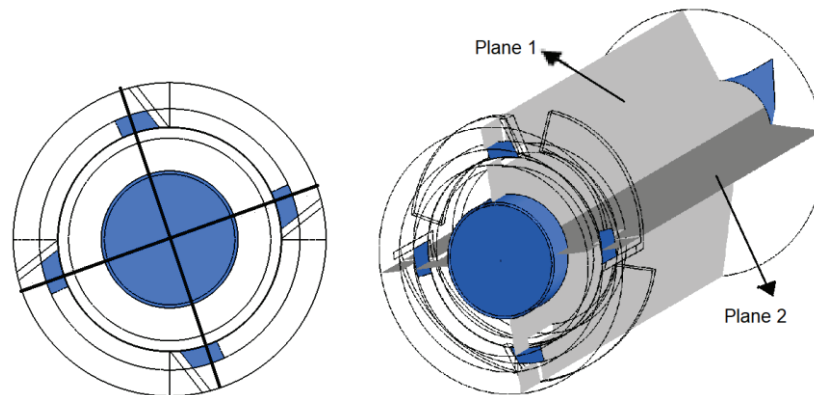


Figure 3-5 Plane 1 and Plane 2 locations in the Spacers

Figure 3-6 demonstrates velocity contour along Plane-1 and Plane-2 for OSIS and CSIS. By comparing Figure 3-6-b and Figure 3-6-d, it can be concluded that the CSIS recirculation core speed is higher than OSIS. For instance, the highlighted recirculation core speed in Figure 3-6-d is reduced in Figure 3-6-b. The comparison between Figure 3-6-d and Figure 3-6-c leads us to the conclusion, that the high-speed region area is larger in the CSIS than the OSIS. To quantify the comparisons, several regions are defined in

the spacers. Then the average speed in that region is calculated by using ANSYS CFD-post. The user-defined plans are shown in

Table 3-7.

Table 3-7 indicates that the average velocity in the OSIS is less than the CSIS for eight different regions of spacers.

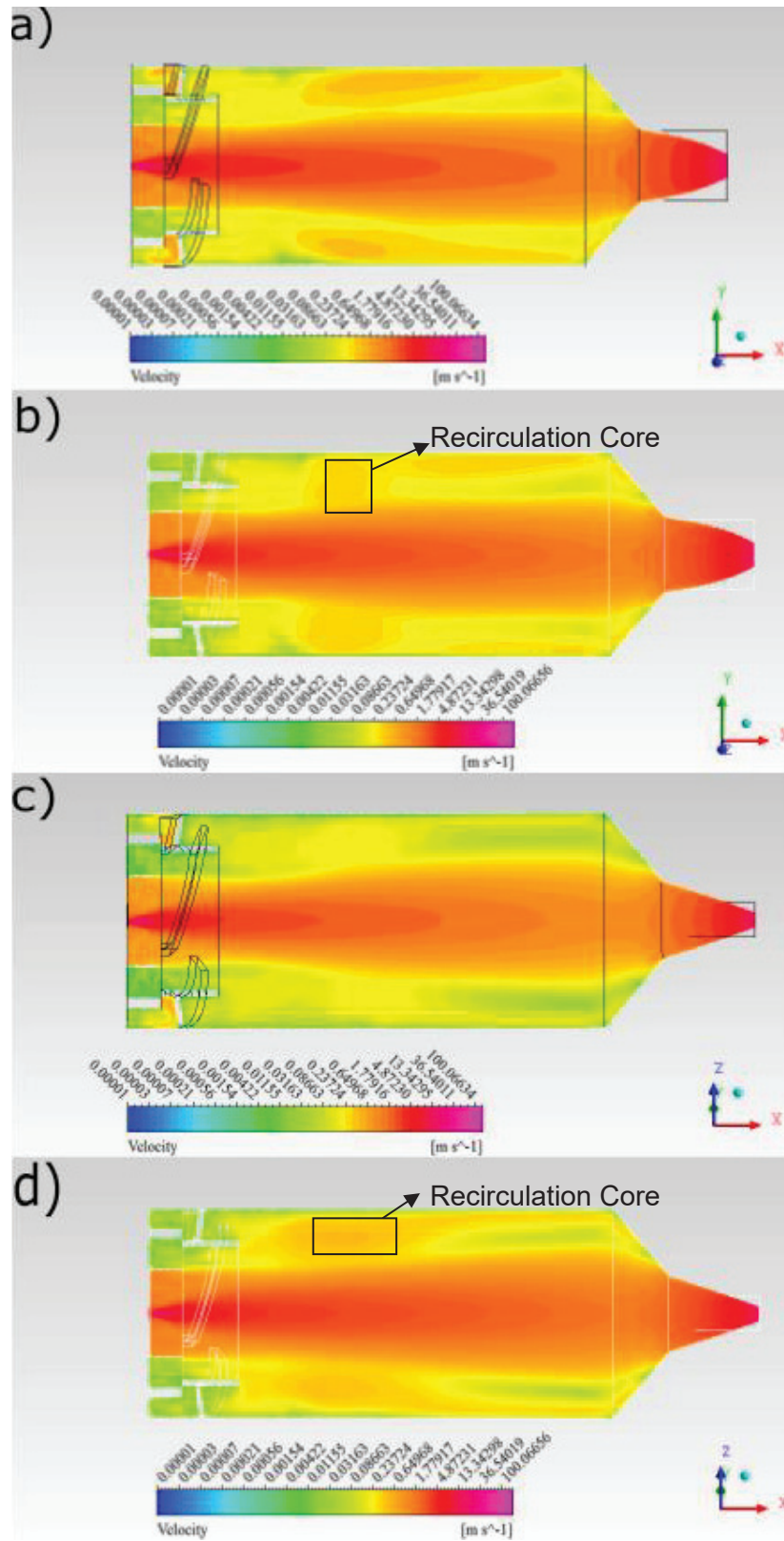
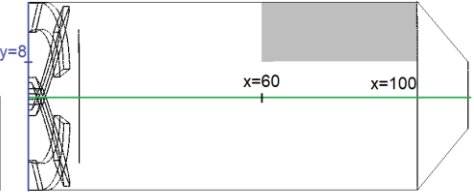
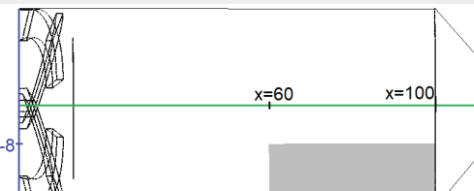
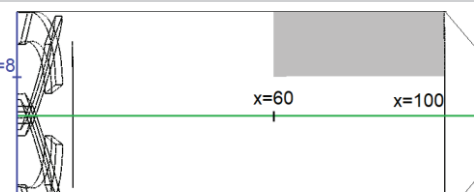
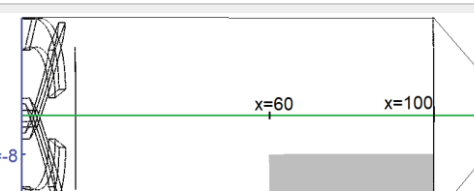
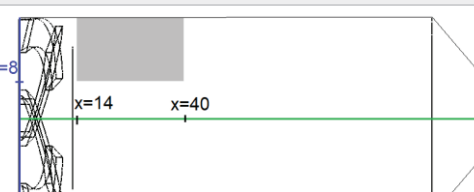
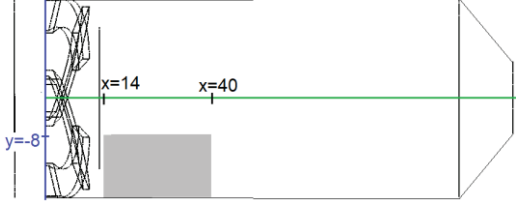
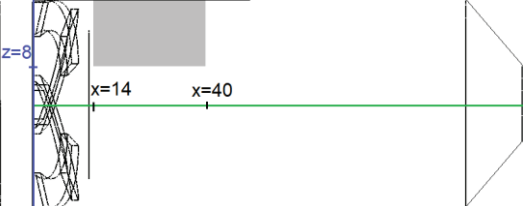
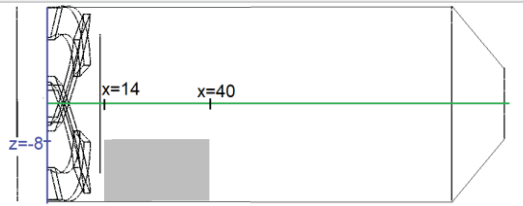


Figure 3-6 Velocity contour of a) OSIS in plane-1 b) CSIS in plane-1 c) OSIS in plane-2 d) CSIS in plane-2



**Table 3-7 Average Velocity on defined locations**

Plane Location	Ave Velocity		Difference %	Plane size (cm <sup>2</sup> )	Plane Location
	OSIS (m/s)	CSIS (m/s)			
	0.2823	0.2992	5.98	320	Plane1
	0.2753	0.2934	6.57	320	Plane1
	0.3056	0.3131	2.45	320	Plane2
	0.3092	0.3191	3.20	320	Plane2
	0.1721	0.1898	10.28	208	Plane1

	0.1784	0.1855	3.98	208	Plane1
	0.1478	0.1749	18.33	208	Plane2
	0.1397	0.1876	34.28	208	Plane2

In Figure 3-7 the velocity streamlines of OSIS and CSIS are shown. Streamline command in ANSYS generates the lines which are tangential to the local velocity vector of a particle inside a domain or specified plane [118]. Figure 3-7-b, four recirculation regions, that are located on the lower side and upper side of the spacer, are transfigured in Figure 3-7-a. This change in shape is most likely caused by secondary inlets flow. Although Ricardo claimed that recirculation zones trap small size particles and reduce drug delivery[67], Sapsis and Haller mathematically proved the existence of regions, called scatter regions, where particles can escape from the recirculation zones [119]. Moreover, Wang introduced a parameter that affects particle escape rate in scatter regions [120]. The streamlines radius has a reverse relationship with particle escape rate. In other words, particles moved out from the recirculation zone when the streamlines curvedness increased. By comparing Figure 3-7-b and Figure 3-7-a, it can be observed in that the streamlines curvedness of two recirculation regions in comparison with Figure 3-7-a where the secondary inlets are open. As a result, the scape rate of scatter regions are increased in OSIS, therefore the particle deposition in spacer reduces.

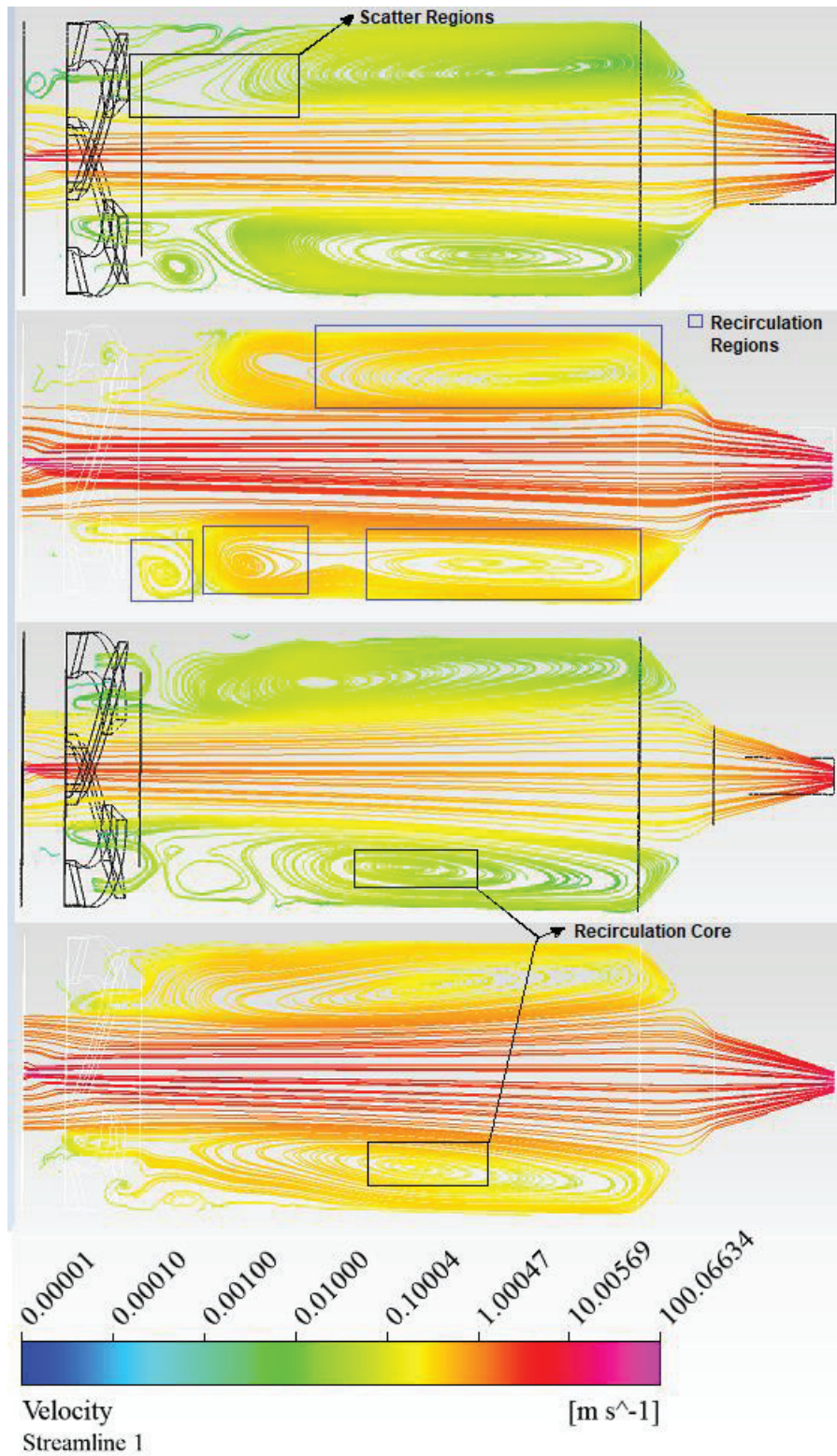


Figure 3-7 Velocity streamlines of a) OSIS in plane-1 b) CSIS in plane-1 c) OSIS in plane-1 d) CSIS in plane-2

Moreover, Figure 3-7 exhibits that recirculation regions' core speed reduces when the secondary inlets are open. Fine particle escape rate has a reverse relationship with recirculation region core speed [120]. Velocity streamlines in Figure 3-7-a reduce in comparison with Figure 3-7-b streamlines velocity. Similarly, this pattern can be seen in Figure 3-7-c and Figure 3-7-d. Therefore, the particle delivery in OSIS can be improved, since the escape rate has increased by lowering recirculation core speed.

### **3.4. Conclusion**

CFD result indicated that OSIS delivered higher FPP than CSIS, while CPP was reduced when the secondary inlets were set to open. Moreover, drug deposition in spacer was improved in OSIS in comparison with CSIS. Fine particles drug delivery was improved 6% in OSIS, and total drug delivery increased 6.47% when the secondary inlets were open. As explained in chapter one, an ideal VHC is an add-on device used with pMDI to increase drug delivery, reduce drug deposition in the patient mouth, and overcome inhalation coordination with spray actuation shortcomings. Based on the ideal spacer definition, OSIS is a better VHC than CSIS.

To investigate the effect of secondary inlets on spacer flow, streamlines and contours of OSIS and CSIS were compared. The result indicated that the recirculation area curvedness and size were changed. Moreover, recirculation's core speed was reduced when the secondary inlets were open. Our simulation showed that the OSIS had less velocity in various regions than the CSB spacer. According to Wang et. al, if the recirculation area velocity increase, the particles need higher velocity than the vortex region to skip from it [120]. Therefore, the patient's inhalation flow rate may not be enough to take the drug particles out of the recirculation area. Recirculation radius and core speed velocity have a reverse relationship with particle escape rate from the recirculation region. Therefore, it can be concluded that spacer drug delivery can be improved by changing the flow inside the spacer. In other words, one can increase drug delivery by reducing the curvature radius and core speed of the recirculation region, rather than completely reducing the recirculation region's size.

## **Chapter 4.**

### **Experimental Study**

#### **4.1. Objective**

To validate numerical simulation, this thesis conducted several experiments to study the effect of static blades and secondary inlets on spacer drug delivery. In this chapter, a cascade impactor device will be introduced which was utilized for conducting the experiments. Moreover, the experiment procedure that is designed based on the Canadian Standard [121] will be described. Later in this chapter, the Ultra Violet-Visible Spectrometer's (UV-Vis) principle will be explained. Then, the drug collected by the Cascade impactor is measured by the UV-Vis method, and the result will be reported at the end.

#### **4.2. Cascade Impactor**

Cascade impactor is a device to measure the aerosol size distribution which was invented in 1945 [122]. The device consists of three main components including an induction tube, plates, and stages. The induction tube is a 90-degree bent tube that connects a spacer or pMDI to a cascade impactor. The stage is housing for the plate, and it has several orifices on its surface. The orifices are designed to only pass particles smaller than a specific number (Figure 4-1), and particles larger than the designated range deposit on the plate, and the rest of the aerosol pass through the orifices toward the next stage. [123]. Cascade impactor stages vary between 3 to 8, and Anderson Cascade impactor has eight stages. In Figure 4-1 the particle size range which is collected in each stage is shown. The particles deposition in each plate depends on several factors including[124]:

- the airstream velocities and the character of the jet airflow
- the orifice sizes
- the aerosol particle shape, size, and density

- the air viscosity
- Distance between the orifice and collector plate and the length of the orifice



Figure 4-1 Anderson cascade impactor

### 4.3. Experiment Setup and Procedure

VORTEX drug delivery was measured in two conditions includes the secondary inlets are open and close. To examine the repeatability of data, OSIS and CSIS were tested three times each. Adult PARI VORTEX® were used during the experiments and were washed prior to the tests based on manufacturer instruction. They were left vertically to drip dry at room temperature. To study the CSIS drug delivery, a pMDI adaptor was designed to replace the VORTEX pMDI cap which has four secondary inlets. The adapter was made of silicon by using the injection molding method (Figure 4-2).





Figure 4-2 CSIS Designed pMDI adaptor

The experiment setup is shown in Figure 4-3. A vacuum pump was connected to an Anderson cascade impactor, and it drew air with a constant flow of 28.7L/min. The VORTEX was connected to the cascade impactor by the induction tube. Salbutamol (Ventolin, HFA 100mg/puff) was employed in the experiments, which was connected to the spacer by the pMDI adaptor.

The test procedure initiated with starting the pump and shaking the pMDI well before the actuation. Three puffs were injected into waste before connecting it to the spacer. A 30-second gap was needed between the first actuation to the spacer and starting the pump. In the next step, pMDI was connected to the spacer and actuated 20 times with a gap of 5 seconds. The pump remained on for 30 seconds after the last puff. This test procedure was the same for OSIS and CSIS. The test was repeated a total number of six times with three Ventolin (HFA 100mg/puff). For each inhaler VORTEX was tested once with the original pMDI adaptor and once with the silicon pMDI adaptor (Figure 4-2) to study open and close secondary inlets, respectively.

pMDI adaptor

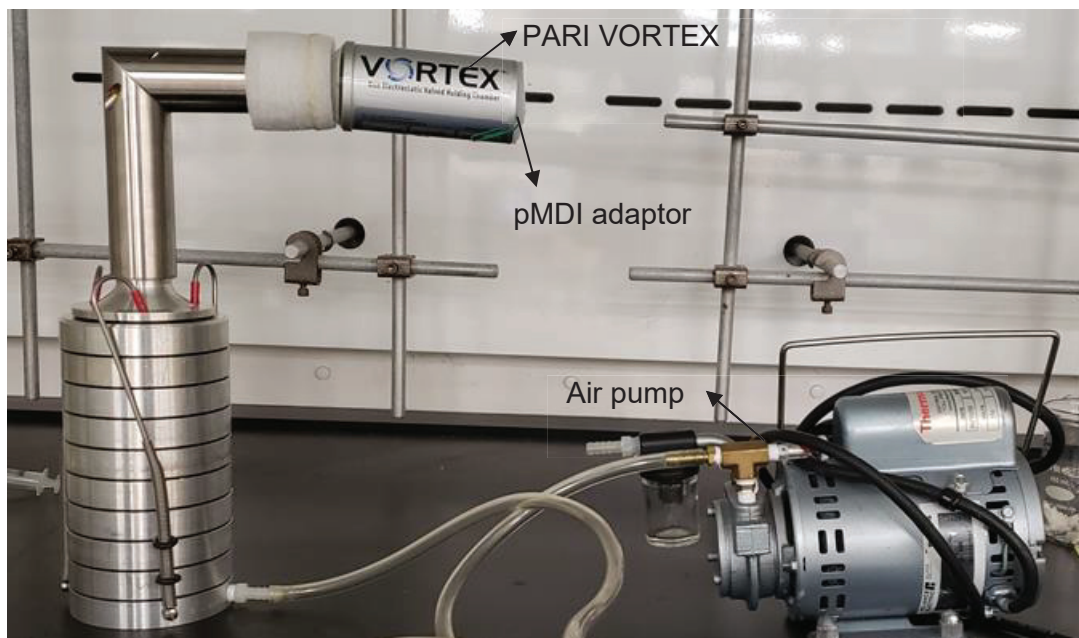


Figure 4-3 Experiment setup for the effect of stator blades in particles size

#### 4.4. Drug Collection and Measurement

After each test, the experiment setup was disassembled, and we collected the deposited drug on the cascade impactor, the inhaler body, and the spacer body by washing parts with a solution. The solution consisted of %50 v/v methanol 50% v/v HPLC water. Disposable pipettes were employed to wash parts. Every time a pipette touched a part, it was disposed, and replaced with a new one (Figure 4-4-b). To collect deposited particles on plates (Figure 4-4-a), they were placed into Petri dishes with 20ml of the solution. Then Petri dishes were shaken with a shaking machine for 15 minutes at 100 rpm while they were floated in solution. Each test had nine samples including Inhaler's body, Spacer, Induction tube, Stage 0-2, Stage 3, Stage 4, Stage 5, Stage6, and Stage 7.





Figure 4-4 a) Deposited drug in cascade impactor plate b) washing cascade impactor stage

#### 4.4.1. Ultraviolet-Visible Spectrophotometer

To measure the particle presented in each sample, we employed Ultraviolet-Visible (UV-Vis) Spectrophotometry method. The UV-Vis spectrometer passes a single (Figure 4-5) with the wavelength of 180nm to 1100nm, which includes the ultra violet wavelength (170nm-380nm) and visible wavelength (380nm -780nm), through a sample [125]. When the light passes through the sample, it may absorb some wavelengths (captivated wave) and transfer the rest. The captivated wave depends on the nature of the material, since absorbed wave energy is used to promote the excited electron to a higher-level energy orbital [126]. The transmitted light passes through a dispersing element which divided the light into different wavelengths. In the last stage, the spectrometer measures the intensity of each wavelength.

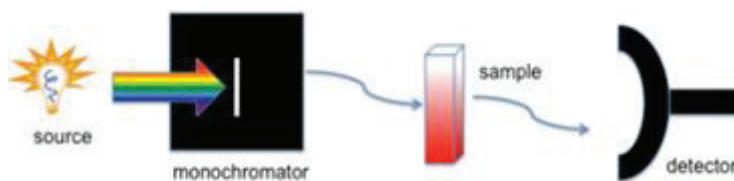


Figure 4-5 Illustration UV-vis instrument [126].

We used a single beam spectrometer Agilent Cary 60 UV-Vis (Figure 4-6-b) to measure the drug particles in each collected sample. A reference sample was necessary to generate the calibration to relate the measured absorbency to the concentration of salbutamol. To generate such reference, a solution of 50% v/v methanol 50% v/v HPLC water was prepared. In a single beam UV-Vis, the reference should be measured first, then the drug concentration in a sample is measured.

Two cuvettes (Figure 4-6-a) were used in sampling measurement, and they were washed with reference solution (50% v/v methanol 50% v/v HPLC) prior to the test. One of them use to measure the reference solution, the other one was employed to measure the drug concentration of nine samples. The second cuvette, which was used for sample measurement, was washed between each sample measurement. It was washed three times with HPLC water, then it is rinsed with reference solution (50% v/v methanol 50% v/v HPLC).

The measurement procedure initiated with the reference solution placement into the machine (Figure 4-6-a). The absorbed wavelength was measured and set to zero. Then the first sample was poured into the second cuvette and placed into the machine. Each sample was measured three times with three wavelengths of 220nm, 226nm, and 276nm. Between each sample measurement, the reference solution was measured and set as zero.

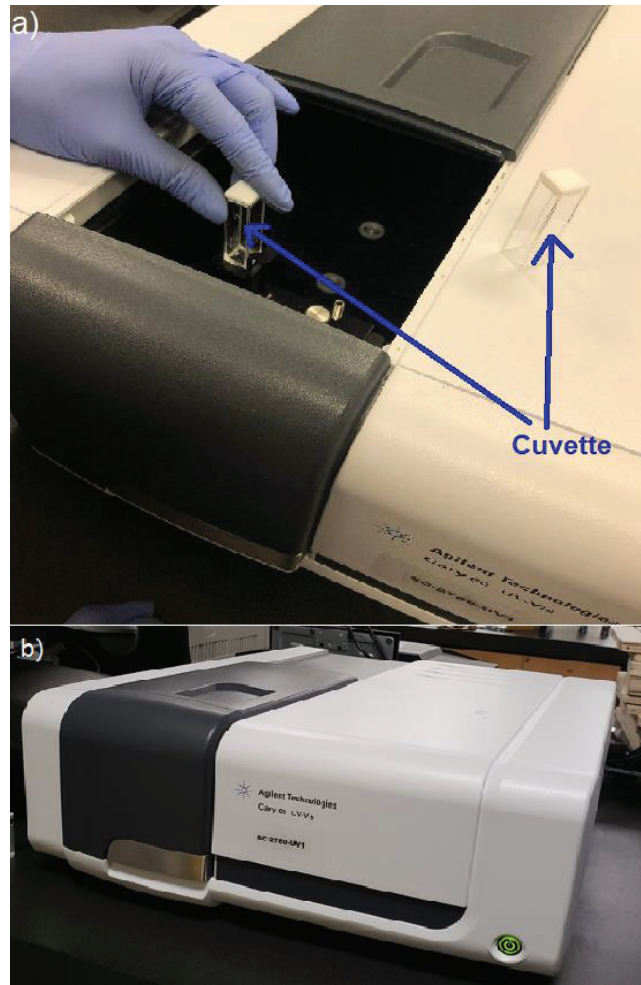


Figure 4-6 a) Placing a sample into UV-Vis b) Agilent Cary 60 UV-Vis

## 4.5. Result and Discussion

The data collected from experiments is shown in Figure 4-7. The bar chart illustrates the average drug deposition percentage on each stage of cascade impactor for CSIS and OSIS. The particle fraction was calculated by dividing the recovered drug in each stage by the total recovered drug in each spacer. In terms of drug deposition in the spacer, the combination of the salbutamol pMDI and the PARI VORTEX with the original pMDI cap (OSIS) was higher in comparison with PARI VORTEX with silicon pMDI cap (CSIS). The delivered dose fraction to the impactor was 42.87% for OSIS and 38.13% for the CSIS. Moreover, the total drug deposited on the induction tube was reduced by 4.8% when the secondary inlets are open. The substantial reduction in OSIS's delivered coarse particles in comparison with CSIS can be observed in drug deposition percentage of the

induction tube, and stage 0-2. The coarse particles are particles larger than  $4.7 \mu m$ , and has the greatest likelihood to deposit in the patient mouth [32]. Therefore, reducing delivered coarse particles is one of the advantages of OSIS over CSIS. Moreover, the drug deposition in cascade impactor stages 3, 4, and 5 increased when the secondary inlets were open. This indicates that OSIS showed a better performance in fine particles ( $1.1-4.7 \mu m$ ) drug delivery. In terms of Extra-Fine Particle (EFP) drug delivery, experimental result indicated that there is not a meaningful difference between OSIS and CSIS. It was observed that the EFP are generally exhaled, and are not absorbed by the lung [32]. Therefore, they don't have a crucial rule in asthma treatment.

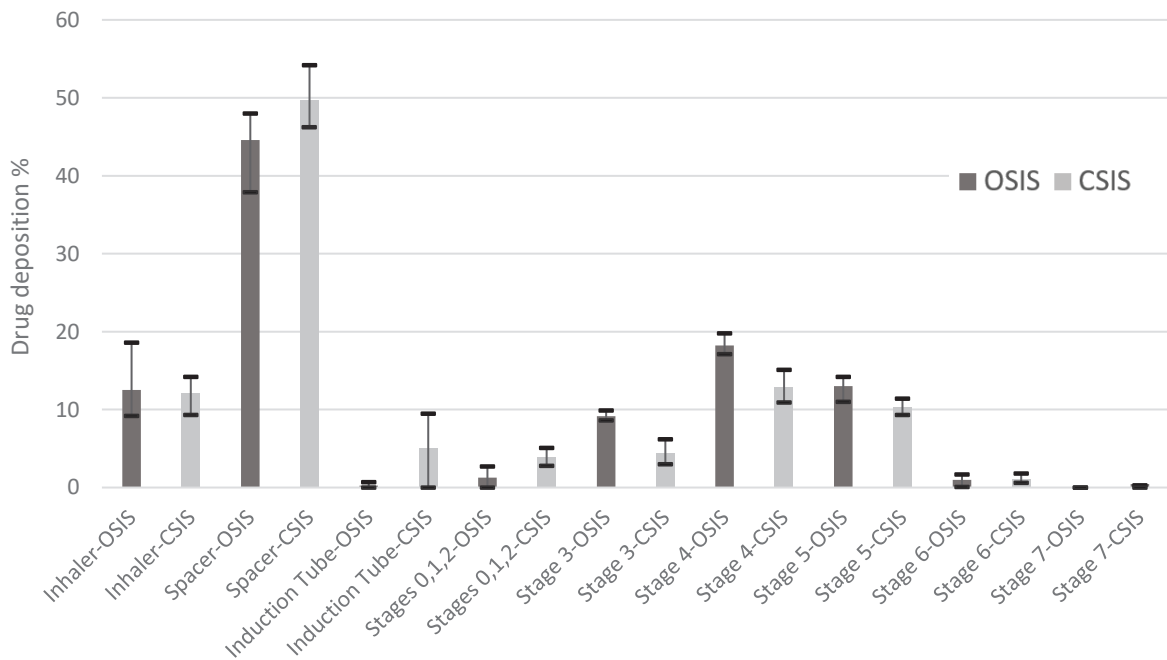


Figure 4-7 Particle deposition fraction (recovered drug in each stage is divided by the total recovered drug in each spacer) in OSIS and CSIS.

Figure 4-8 illustrates a comparison between OSIS and CSIS drug delivery in experimental and computational studies. Particles are categorized into three groups including Coarse Particle Percentage, Fine Particle Percentage, and Extra-Fine Particle Percentage. Figure 4-8 indicated that secondary inlet improved the spacer total delivered drug by 6.4% and 11.6% in CFD and experiment study, respectively. Moreover, the in-vitro and CFD study showed that OSIS delivered a higher percentage of fine particles in comparison with CSIS. The experimental and numerical results indicate that the CPP and

drug deposition in spacer reduces in OSIS in comparison with CSIS. Furthermore, the CFD and experiment result shows that FPP is higher in OSIS than CSIS. However, the difference between the two results may be caused by experiment errors which include:

- Difference between the air pump nominal flow rate and its actual flow rate
- UV-Vis device errors
- Human errors
- Simplifications for simulation due to software limitations

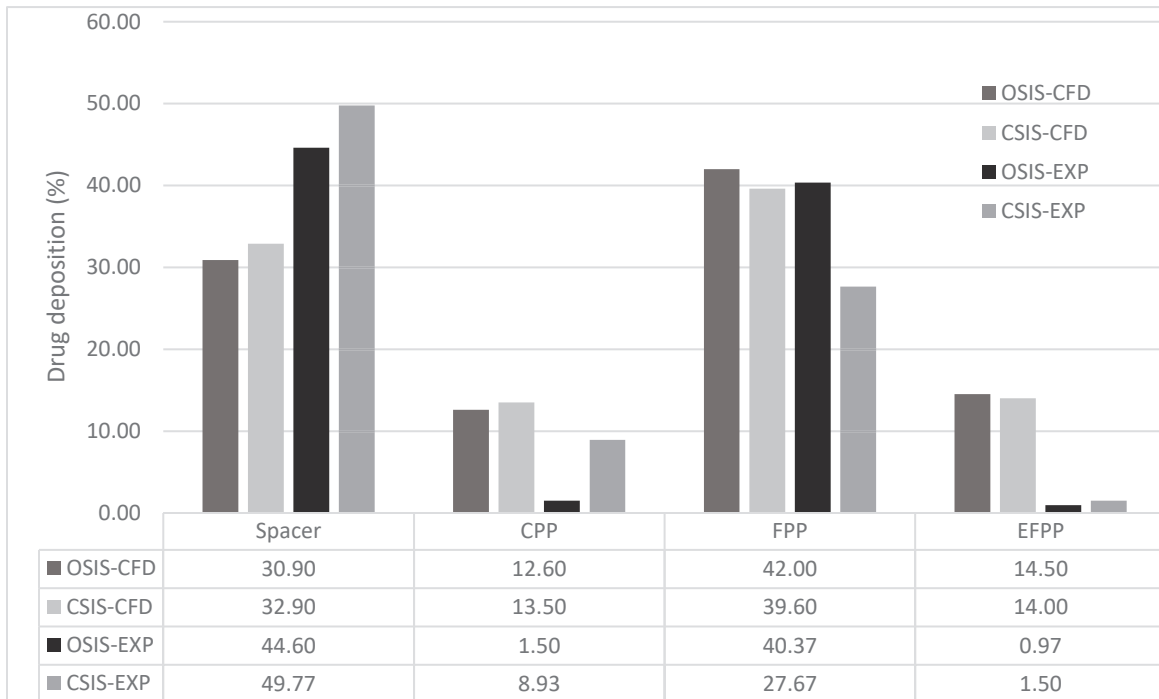


Figure 4-8 Numerical and Experimental results for drug deposition in OSB and CSB spacers

## 4.6. Conclusion

The experiments validated the simulation result, and both verified that the open secondary inlets improve drug delivery. It was observed in chapter three that the secondary inlet changes the flow rate inside the spacer which has an effect on the spacer's drug delivery. In this chapter, it was shown that the spacer's drug delivery can be

enhanced by having a secondary flow. It was shown that the open secondary inlets increase the delivered fine particle percentage, and reduce delivered coarse particle percentage. However, the secondary inlet does not affect delivered extra-fine particles.

## **Chapter 5.**

### **Design Optimization**

#### **5.1. Introduction**

In chapters three and four, the role of the secondary inlet in spacer drug delivery was discussed. It was shown that the open secondary inlets increase total drug delivery and fine particle delivery. In this chapter, the spacer drug delivery, and the delivered particle sizes will be optimized. Since the flow streamlines change near the blade and they have a relationship with blade geometry [127], both secondary inlet geometry and static blade's geometry parameters are set as variables in the optimization. To initiate the optimization, first, the available optimization methods in ANSYS software will be reviewed. Later, the secondary inlet and static blade's geometrical parameters will be defined for the optimization process, and the optimization setup in ANSYS will be explained. In the last stage, the optimization result will be discussed.

#### **5.2. Optimization Method**

ANSYS provides two methods for optimization including direct optimization and response surface optimization (Appendix A). In this thesis, the direct optimization method is used, since the response surface optimization methods available in ANSYS are not suitable for this multi-objective optimization with manufacturable inputs [128].

##### **5.2.1. Direct Optimization in ANSYS**

ANSYS-directed optimization solves the simulation and calculates the optimum point using the design points' objectives values [128]. This method is found suitable for optimizing spacer since the number of blades is discrete value and some of the available direct optimizations in ANSYS are suitable for discrete inputs. ANSYS provides three direct methods for multi-objective optimization including Screening, Adaptive Multi-Objective, and Multi-Objective Genetic Algorithm (MOGA). Screening method is categorized as the fast optimization method in ANSYS, and it is typically used to generate the primary set of points for a preliminary design. Adaptive multi-objective is categorized

as moderate pace optimization methods in ANSYS, and it is suitable only for continuous input parameters. Multi-Objective Genetic Algorithm (MOGA) is an optimization method to find the global optimum by using the natural selection mechanism. MOGA is suitable for all types of inputs, and it usually takes longer than the other two methods. MOGA has several features includes [129]:

- Employing a set of design points instead of a single design point.
- Using the objective function value as a reference for optimization direction instead of using first derivatives.

MOGA uses three operators for optimization including reproduction, crossover, and mutation. Reproduction occurs when the design point moves to the next generation without any changes [128]. The fitness function decides which points can move forward to the next generation. The fittest point has a higher probability to move the next population without any changes. Crossover selects two points as parents and by mixing their string generates two children which will be used in next generations. Figure 5-1 shows crossover types for discrete input. The crossover can occur in one point, two-point, and uniform methods. In Figure 5-1 one-point crossover showed that the first two strings of the one parent are exchanged with the first two strings of another parent. Therefore, two kids are generated with different combinations with their parents. The same method applies to two points crossover and uniform crossover. The crossover operation for continuous value is defined in Equation 5-1.

Equation 5-1

$$child1 = a * parent1 + (1 - a) * parent2$$

$$child2 = (1 - a) * parent1 + a * parent2$$

Where  $a$  is a random number on the interval [0,1]. By multiplying  $a$  to the first parent and  $(1 - a)$  to the second parent, the first child is generated. This method applies to generate the second child as well.



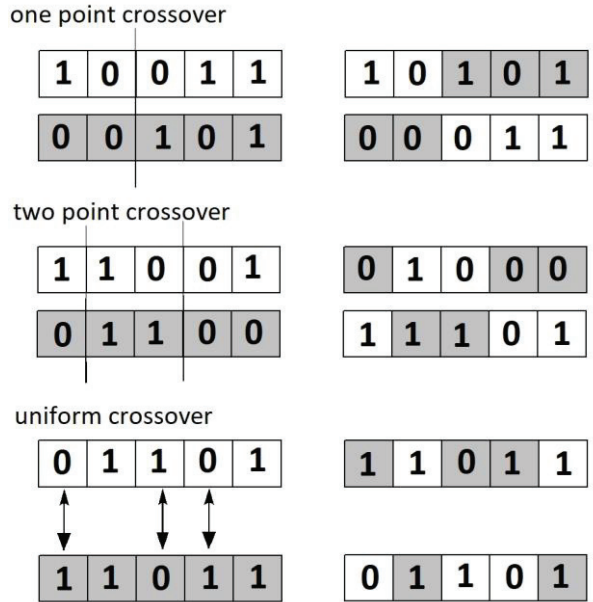


Figure 5-1 Genetic Algorithm crossover operation types for discrete parameters

Mutation operation changes one or two strings of a design point. Therefore, completely new genomes are added to the population. This operation reduces the chance of finding the local minimum instead of the global minimum. Mutation operation changes the value of 1 or more strings of a parent and generates a new child for next population. Figure 5-2 shows mutation operation for a discrete parameter, where the mutation operator changed the third and fourth-strings values of the parent and generated the child.



Figure 5-2 Genetic Algorithm mutation operation for discrete parameters

The mutation operation for continuous values is defined in Equation 5-2.

Equation 5-2

$$Child = Parent + (UpperBound - LowerBound) * \delta$$

Where  $\delta$  represents a small variation that is calculated from the polynomial distribution.

The evolutionary algorithm optimization continues creating new generations until it reaches the maximum iteration or converges at the set value. The genetic algorithm process is shown in Figure 5-3.

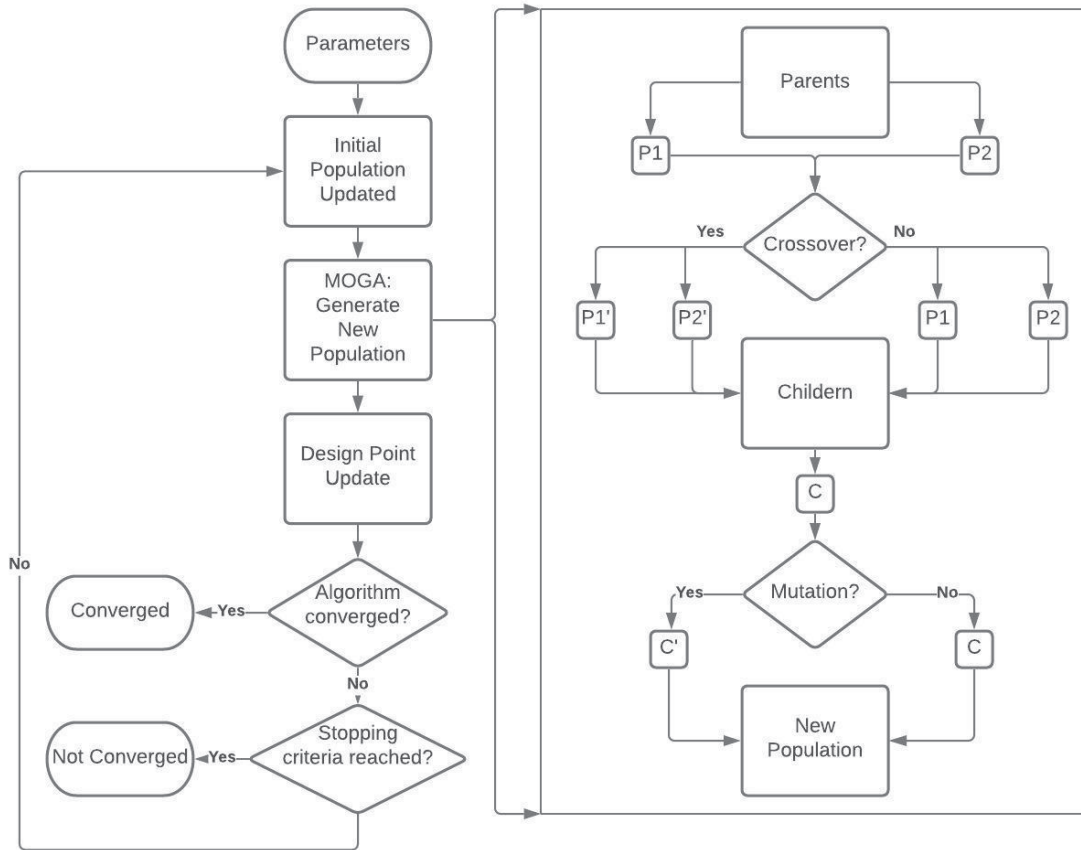


Figure 5-3 Multi-Objectives Genetic Algorithm workflow [128]

### Non-Dominated Sorting Genetic Algorithm-II (NSGA-II)

K. Deb et al. for the first time introduced the Non-Dominated Sorting Genetic Algorithm-II (NSGA-II) [130]. In this method, after the initial population ( $P_1$ ) and the second population ( $P_2$ ) are generated, they will be combined in a group ( $Q$ ). If the  $P_1$  and  $P_2$  size is  $N$ , then  $Q$  size is  $2N$  [131]. Then non-domination sorting will be performed on the  $Q$  population. The solutions of the population of  $Q$  can be subcategorized into smaller groups which are called Pareto fronts [132]. The non-dominated sorting uses Pareto concept to rank fronts [133]. Pareto optimal is a set of solutions for a multi-objective optimization where its objectives functions have conflicts. In multi-objective optimizations usually,

objective functions conflict with each other. Therefore, these types of optimizations end up with a set of solutions (Pareto Optimal) rather than a single answer [133]. If the objective functions of a multi-objective optimization do not have contrast, therefore any optimization methods which apply to single-objective functions can be employed. The first Pareto front is consisting of solutions that are not dominated by any other solutions in populations Q. Each solution in the front  $1 + i$  is at least dominated by one solution from the previous fronts. A Solution x dominate solution y if and only if [132]:

Equation 5-3

$$\begin{cases} \forall i \in 1, \dots, M : f_i(x) \leq f_i(y) \\ \exists j \in 1, \dots, M : f_j(x) < f_j(y) \end{cases}$$

Where M represents the number of conflicting objective functions. By using this concept, the population Q can be divided into two subsets.



Figure 5-4 Non-dominated sorting for a multi-objective function [132]

Figure 5-4 shows a two-objective functions population which is sorted into three ranks. None of the solutions that belong to a rank can dominate any solution from the same rank.

In NSGA-II method after the non-dominated sorting, the non-dominated fronts will move forward to the next populations ( $R$ ). This process starts with the best non-dominated fronts and then moves to the next best non-dominated solution. This process continues until the  $R$  size is equal to  $N$ . Since, the size of the  $Q$  is  $2N$  only half of the design points are able to move forward. The remaining design point will be deleted. In the early iteration of the optimization process, the NSGA-II method does not make a huge difference in the optimization process. However, in the last stages, the importance of the NSGA-II will be observed more clearly. The NSGA-II workflow procedure is shown in Figure 5-5.

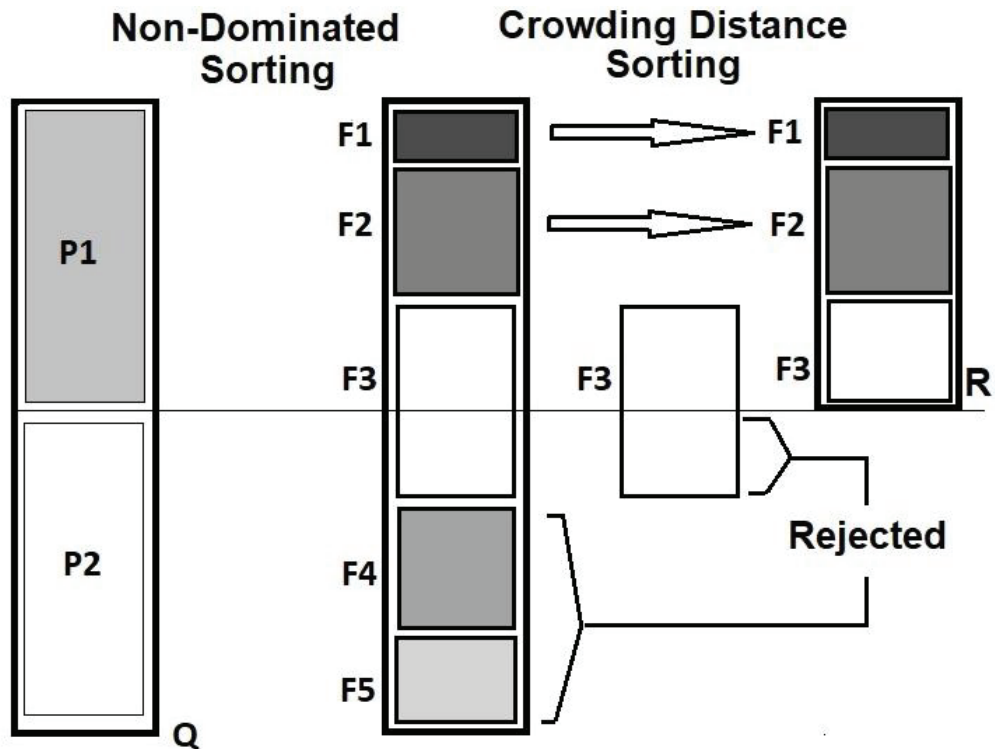


Figure 5-5 NSGA-II workflow

As it was shown in Figure 5-5, there is not enough spot for the whole member of group  $F3$  to move to  $R$ . In this case, the Crowding Distance Sorting method helps to pick the best member of that front. The crowding distance metric is used in NSGA-II. The distance procedure is:

Step 1: define  $d_i=0$  for each  $i$ .

Step 2: Sort the solutions for each objective function in the front.

Step 3: Assign the boundary solutions crowding distance equal to infinity. then Calculate the crowding distance for the other solutions by:

Equation 5-4

$$d_{I_j^m} = d_{I_j^m} + \frac{f_m^{I_{j+1}^m} - f_m^{I_{j-1}^m}}{f_m^{\max} - f_m^{\min}}$$

Where  $m$  represents each objective function and  $l$  is the number of the solution in the front and  $j=1,2,\dots, l$ .  $f_m^{I_{j+1}^m} - f_m^{I_{j-1}^m}$  is the difference between the value of two solution points that are neighbors of  $I_j^m$  solution point.  $d_{I_j^m}$  is initially equal to zero for non-boundary solutions. Figure 5-6 demonstrates the example of crowding distance calculation for two objective functions of  $f_2$  and  $f_1$ . The solution points with a higher cuboid distance move to the  $R$  population (Figure 5-5).

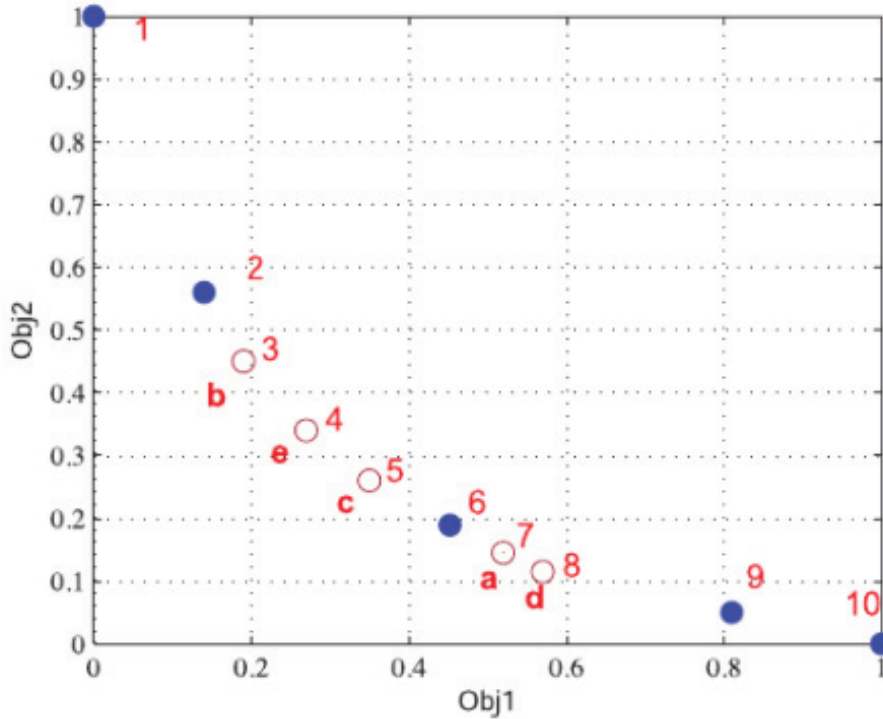


Figure 5-6 Crowding distance Calculation for two objective functions [134]

Figure 5-6 shows a Pareto front which consists of ten solutions of two objective functions optimization. The solutions with the highest crowding distance value can move

to the next generation [134]. As explained earlier boundary solutions crowding distances are equal to infinity which placed them at the top of the list to move to the next generation. In Figure 5-6, solution 7 has the smallest crowding distance amount other solution of the front. There it will be deleted from the list and then crowding distance is calculated again for the remaining 9 solutions. Then the crowding distance is calculated again, and this time the solution number 3 has the smallest crowding distance among other solutions. This process is repeated until the 5 points of 1, 2, 6, 9, and 10 are chosen as solutions that can move to the next generation ( $R$  population-Figure 5-5). The number of solutions that transfer to the  $R$  population depends on the number of available spots on  $R$  population.

In this study, the NSGA-II is chosen to calculate the optimum design for static blades, since this method is suitable for multi-objective optimization. Moreover, the crowding distance is an extra operation tool that is utilized besides mutations, reproductions, and crossover.

### **5.3. Optimization Parameters**

To maximize the drug delivery and minimize the delivered particle size, first, the input variables are needed to be defined. The secondary inlet and the static blade's geometries are chosen as the input variable. The secondary inlet location, opening, and corner angle are chosen to be studied. Therefore, secondary inlet height, angle, location, and corner angle are set as input parameters. The number of inlets (number of static blades) is another crucial input parameter that is defined, and it is named as the main angle in Figure 5-7. The blade angle, which is defined as the angle between the x-axis and blade edge, is also set as another input parameter.

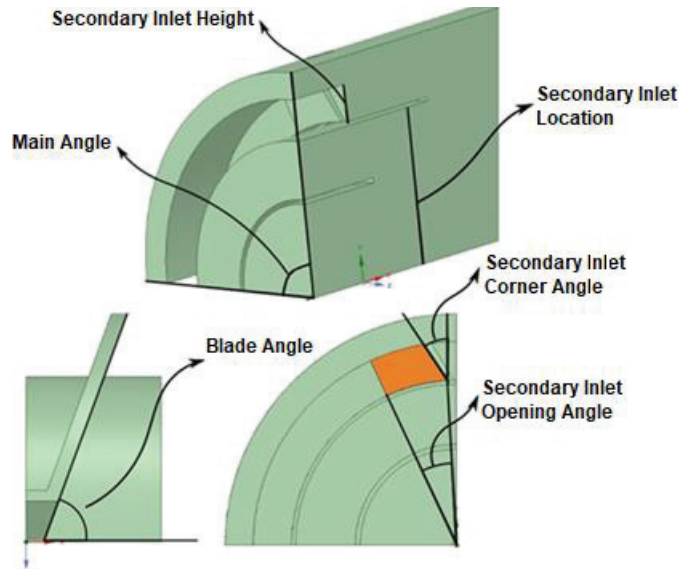


Figure 5-7 Optimization Input parameters

As explained earlier, the ideal spacer is an add-on device used with pMDI to increase the drug delivery, reduce the delivered CPP, and enhances the delivered FPP. Therefore, the main goal of this optimization is to find the spacer design with the highest drug delivery and the lowest average particle size. To do so, the total delivered drug and average particle size at the outlet are set as output parameters.

## 5.4. ANSYS Setup

To initiate the optimization, the simulation setup should be set as explained in chapter three. However, a section of the spacer body is simulated to reduce computational cost. The slice degree has the same value as the main angle input parameter which represents the number of secondary inlets in a spacer. Since the valve only has two plane symmetry, it is not considered in optimization geometry. The flow near the valve depends on the shape of the valve and the mechanical properties of its material. Moreover, the available valve in the market has various efficacy and comparison between their efficacy is out of the scope of this thesis. Therefore, in this thesis, it was decided to optimize the VHC body (without the valve). Next, the optimization setup should be defined. The purpose of this study is to design an optimum spacer with the highest drug delivery and minimum average particle size. Therefore, the average particle size at the outlet boundary is set as an objective function. The next objective function measures the spacer drug

delivery percentage which calculates the ratio of drug mass flow rate at the outlet to the injection region. Since the standard optimization problem should be defined as minimizing the objectives functions, the negative function of the total delivered drug is written in Equation 5-5. The optimization formulation was shown in Equation 5-5.

Equation 5-5

minimize

$$f_1 = (\text{salbutamol.Averaged Mean Particle Diameter})@Outlet$$

$$f_2 = -\frac{\text{salbutamol.massFlow(Outlet)} * 2 * \pi * 100}{\text{salbutamol.massFlow(Injection)} * \text{SliceDegree}}$$

Subject to

$$g_1 \geq \text{main angle} \rightarrow (\text{bladeinlet} - 5[\text{degree}]) \geq \text{main angle}$$

$$g_2 \geq \text{inlet height} \rightarrow 23[\text{mm}] - \text{blade's inlet location} \geq \text{blade's inlet height}$$

Where:

$$5[\text{degree}] \leq \text{blade angle} \leq 30[\text{degree}]$$

$$10[\text{degree}] \leq \text{blade's inlet angle} \leq 40[\text{degree}]$$

$$0[\text{degree}] \leq \text{blade's inlet corner angle} \leq 45[\text{degree}]$$

$$1[\text{mm}] \leq \text{blade's inlet height} \leq 10[\text{mm}]$$

$$12[\text{mm}] \leq \text{blade's inlet location} \leq 21[\text{mm}]$$

$$\text{main angle} = x_i[\text{degree}], \quad x_i = 90^\circ, 72^\circ, 60^\circ, 45^\circ, 40^\circ, 36^\circ, 30^\circ$$

Where,  $f_1$  and  $f_2$  represent the average particle size at outlet and total drug delivery percentage respectively. Two constraint functions of  $g_1$  and  $g_2$  are defined to avoid infeasible design. As it is shown in Equation 5-5 main angle is the only discrete input parameter while the other five are all continuous parameters. The MOGA (NSGA-II)



method is chosen with 11 maximum iterations. The convergence stability percentage is set to 7%. The one-point method is selected for the type of discrete crossover, and the number of design points in each population is set at 51.

## 5.5. Result and Discussion

After 9 iterations, the result was converged with 6.78% of convergence stability. 399 design points were generated in 9 populations. The optimization results and the original PARI VORTEX design are compared in Table 5-1. As explained in Non-Dominated Sorting Genetic Algorithm-II (NSGA-II) the optimization result consists of set of candidates points, since NSGA-II uses Pareto optimal concept for multi objective function optimization. The value of particle delivery and mean particle diameters could be slightly different from chapter three (<1%), and it does not impact the overall optimization result. This difference might be the result of eliminating the valve from the spacer. In terms of the number of secondary inlets, all three optimum points have four secondary inlets (main angle 90°) which is the same as the original PARI VORTEX design. Based on Table 5-1 data, the average size of delivered particles was improved in comparison with the VORTEX and the three candidate points. However, the total delivered drug of three optimum designs was lower than the VORTEX.

**Table 5-1 Optimization result**

	Candidate point 1	Candidate point 2	Candidate point 3	VORTEX (OSIS)
Blade Angle [degree]	17.92	9.56	18.91	20
Inlet Corner Angle [degree]	11.88	11.84	11.90	38
Inlet Angle [degree]	37.60	34.65	34.65	24
Inlet Height [mm]	5.30	5.30	2.85	2.8

Inlet Location [mm]	15.06	15.07	16.91	17.1
Main Angle [degree]	90	90	90	90
Particle Delivery%	65.6	67.2	62	68.8
Drug Mean Diameter [ $\mu m$ ]	5.33	5.58	5.61	7.02

In the next step, the input parameters correlations with the output parameter were studied. Having total delivered drug and mean size of the delivered drug as dependent variables, we conducted a multivalent multiple regression test to find the significance of relationships between variables. The results indicated that only the number of secondary inlets have a significant relationship with the total delivered drug ( $R^2 = .03$ ,  $F(6,348) = 2.64$ ,  $p = .01$ ). The correlational result on the average size of delivered particles showed that four variables including secondary inlets height, corner angle, location, and number of secondary inlets have a significant relationship with the averaged size of delivered drug ( $R^2 = .49$ ,  $F(6,348) = 59.41$ ,  $p < .01$ ). Figure 5-8-a and correlation test showed that the number of secondary inlets and the drug average size in the outlet has a negative significant correlation ( $r(348) = -.18$ ,  $p < .001$ ). Moreover, it was shown that this parameter has a strong positive relationship with the average size of delivered particles ( $r(348) = .65$ ,  $p < .001$ ).

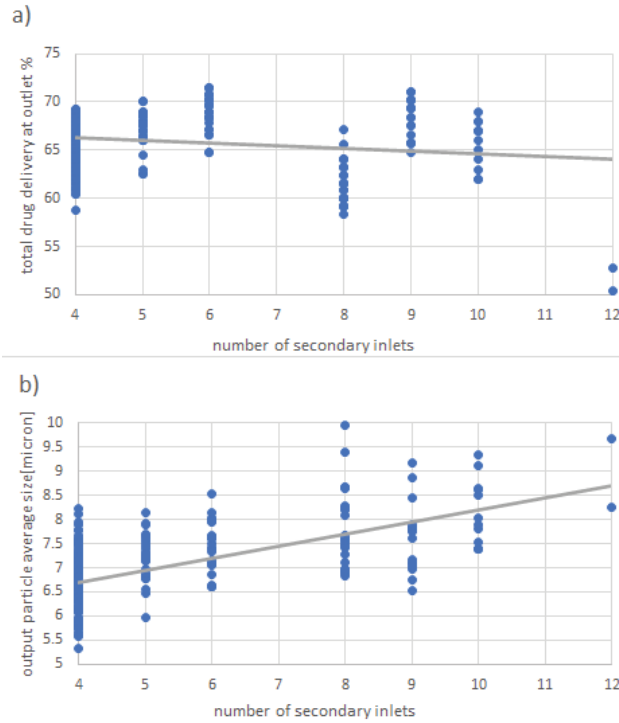


Figure 5-8 Spacer number of secondary inlets relation with a) total drug delivery at outlet b) output particle average size

Figure 5-9-a and correlation test result indicate the secondary inlet height does not have a relationship with the total delivered drug. Figure 5-9-b implies the static blade inlet height has a negative significant correlation with the average particle size at the outlet ( $r(348) = -.18, p < .001$ )

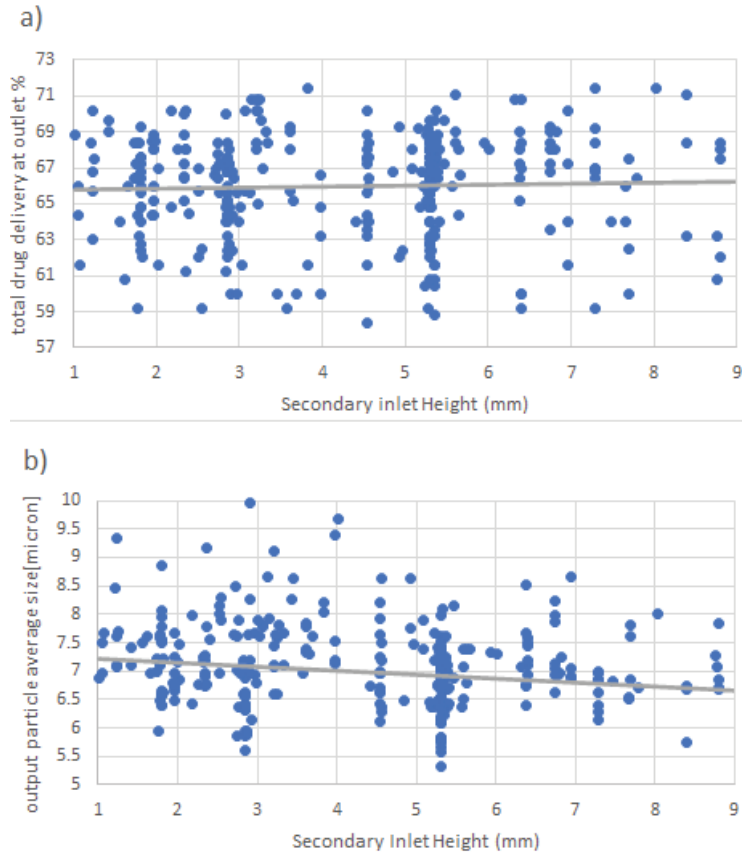


Figure 5-9 Secondary inlet height relation with a) total drug delivery at outlet% b) output particle average size[micron]

Secondary inlet location relation with two optimum functions was shown in Figure 5-10. This parameter has a negative correlation with means particle size at the outlet ( $r(348) = -.08, p < .001$ ) and does not have a significant relationship with the total delivered drug.

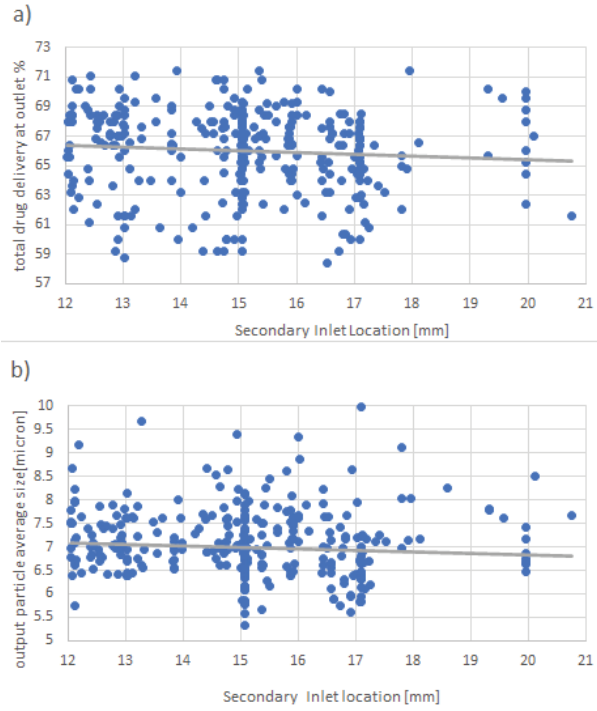


Figure 5-10 Secondary inlet location relation with a) total drug delivery at outlet% b) output particle average size[micron]

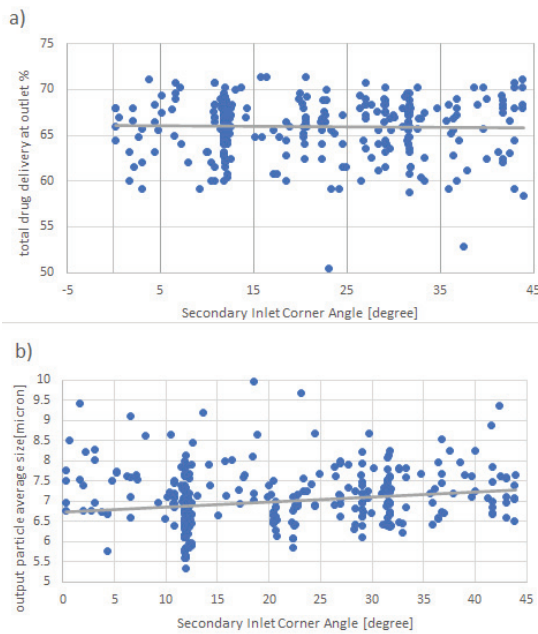


Figure 5-11 Secondary inlet corner angle relation with a) total drug delivery at outlet% b) output particle average size[micron]

The secondary inlet corner angle correlation with output functions was presented in Figure 5-11. The correlation test result indicates that there is a significant positive correlation between this parameter and the average particle size at the outlet ( $r(348) = .43$ ,  $p < .001$ ).

## 5.6. Conclusion

The optimization result reported three design points which their average delivered particles sizes are smaller than the original VORTEX. As explained earlier, the objective functions conflict in most multi-objective optimization. Which was also observed in this optimization. Simulation indicated that the original VORTEX design has higher total drug delivery. Three optimization design points have smaller average particles size at the outlet in comparison with the original VORTEX. The average particles sizes at the outlet of candidate point 1 was improved by 24% in comparison with PARI VORTEX. However, the drug delivery of candidate points 1 reduced 4.6% percentage. The improvement in average particles sizes is more significant and larger than reduction in drug delivery.

We also conducted the correlational test on optimization variables and objective functions. The test showed that the number of secondary inlets has a significant negative correlation with the total delivered drug. The average size of the delivered drug has a significant positive correlation with both secondary inlet corner angle and the number of secondary inlets. Moreover, it has a significant negative correlation with secondary inlet height and secondary inlet location.

## Chapter 6.

### Summery and Future Work

#### 6.1. Summery

PARI VORTEX showed exceptional performance among other VHC, which we showed that it benefits from its unique pMDI adaptor. VORTEX pMDI adaptor has four static blades which are equally spaced, and they have four rectangular shape inlets. In this study, first, the role of these secondary inlets was investigated in a computational study. PARI VORTEX geometry was simulated in ANSYS, and the boundary conditions were defined based on previous studies. The secondary inlets boundary was set as open and closed in two separate simulations, to compare the role of the secondary inlets in spacer performance. OSIS and CSIS streamlines were compared, and their drug delivery was analyzed. The computational study showed that the total delivered drug and FPP increase when the secondary inlets are open. Moreover, the comparison between the OSIS and CSIS indicated that the recirculation region's size, curvedness, and core speed change when the secondary inlets are open. Previous studies showed that the recirculation regions' curvedness and core velocity have a relationship with particle trap rate in spacer. Therefore, it was concluded that the secondary inlets caused the improvement in spacer drug delivery by modifying the recirculation regions' properties. Later, an experimental study was conducted to verify the CFD study result. The experimental result indicated that the spacer performance is improved when the secondary inlets are open. OSIS delivered less CPP and higher FPP than CSIS. In the last stage of this thesis, VORTEX secondary inlets and static blades were optimized. All three optimization candidates' points have four secondary inlets which is same as original PARI VOREX pMDI adaptor. It was shown that three optimization candidates average particles sizes at outlet is smaller than the average particles sizes at PARI VORTEX. The average particle size at outlet was reduced by 24% in one of the optimization candidate points. However, the candidate point 1 drug delivery was reduced 4.6% in comparison with PARI VORTEX. This was expected and understandable, since the objective functions has conflict.

## 6.2. Future Work

Designing a secondary inlet in other locations of the spacer with different designs is highly notable for future study. The recommended location for the secondary inlets is the spacer body where the recirculation regions occur. The CFD study showed that the near the mouthpiece has recirculation regions.

Moreover, in the future, drug simulation can be improved which can help to reduce simulation errors. In this thesis, the drug evaporation and heat transfer equations were not considered. However, Gavtash[135] introduced a new method for simulation drug evaporation. In the future, this method can be used in VHC simulation, and the result can be compared with the current CFD result.

The improvement in the optimization method is another interesting topic for future study. One can improve optimization by changing the objective function to be more specified and targeting the fine particle delivery. In other words, instead of minimizing the average particle size at the outlet, the fine particle percentage at the outlet can be maximized. Furthermore, In the future, the spacer can be optimized with other methods such as connecting MATLAB to ANSYS and using MATLAB as a tool for optimization and ANSYS for simulation. We only used the ANSYS optimization tools for optimization which are limited.

The spacer geometry parameters were considered constant in this study. One can optimize the spacer by considering the spacer and secondary inlet parameters at the same time. The result can be compared with the VORTEX spacer. This helps to understand the effect of secondary inlets and spacer design on flow streamlines in the VHC.



## References

- [1] Public Health Agency of Canada, *Report from the Canadian Chronic Disease Surveillance System: Asthma and Chronic Obstructive Pulmonary Disease (COPD) in Canada*. 2018.
- [2] M. Masoli, D. Fabian, S. Holt, and R. Beasley, "The global burden of asthma: Executive summary of the GINA Dissemination Committee Report," *Allergy Eur. J. Allergy Clin. Immunol.*, vol. 59, no. 5, pp. 469–478, 2004, doi: 10.1111/j.1398-9995.2004.00526.x.
- [3] H. Boutin and L.-P. Boulet, *Understand and Control Your Asthma*. Montreal, CANADA: McGill-Queen's University Press, 1995.
- [4] P. Anderson, "Use of Respimat Soft Mist inhaler in COPD patients.," *Int. J. Chron. Obstruct. Pulmon. Dis.*, vol. 1, no. 3, pp. 251–259, 2006, doi: 10.2147/copd.2006.1.3.251.
- [5] F. Lavorini *et al.*, "Retail sales of inhalation devices in European countries: So much for a global policy," *Respir. Med.*, vol. 105, no. 7, pp. 1099–1103, 2011, doi: 10.1016/j.rmed.2011.03.012.
- [6] C. R. Management, "Choosing the right inhaler for your asthma or COPD patient," pp. 461–472, 2019.
- [7] M. Ibrahim, R. Verma, and L. Garcia-Contreras, "Inhalation drug delivery devices: Technology update," *Med. Devices Evid. Res.*, vol. 8, pp. 131–139, 2015, doi: 10.2147/MDER.S48888.
- [8] J. B. Fink, R. R. T. Faarc, B. K. Rubin, and M. Mba, "Problems with inhaler use1360.full," pp. 1360–1375, 2005, Accessed: Feb. 20, 2018. [Online]. Available: <http://rc.rcjournal.com/content/respcare/50/10/1360.full.pdf>.
- [9] C. Kofman and A. Teper, "Usefulness of Nonvalved Spacers for Administration of Inhaled Steroids in Young Children with Recurrent Wheezing and Risk Factors for

- Asthma,” *Can. Respir. J.*, vol. 2018, pp. 1–5, 2018, doi: 10.1155/2018/3095647.
- [10] S. P. Newman, “Spacer devices for metered dose inhalers,” *Clinical Pharmacokinetics*, vol. 43, no. 6, pp. 349–360, 2004, doi: 10.2165/00003088-200443060-00001.
- [11] R. Buhl, “Local oropharyngeal side effects of inhaled corticosteroids in patients with asthma,” *Allergy Eur. J. Allergy Clin. Immunol.*, vol. 61, no. 5, pp. 518–526, 2006, doi: 10.1111/j.1398-9995.2006.01090.x.
- [12] D. RM *et al.*, “A novel, versatile valved holding chamber for delivering inhaled medications to neonates and small children: laboratory simulation of delivery options.,” *Respir. Care*, vol. 55, no. 4, pp. 419–426, 2010, [Online]. Available: <http://search.ebscohost.com/login.aspx?direct=true&db=cin20&AN=105183038&site=ehost-live>.
- [13] H. W. Kelly *et al.*, “Evaluation of particle size distribution of salmeterol administered via metered-dose inhaler with and without valved holding chamber,” *Ann. Allergy, Asthma Immunol.*, vol. 87, no. 6, pp. 482–487, 2001, doi: 10.1016/S1081-1206(10)62261-2.
- [14] L. Slator, D. Von Hollen, D. Sandell, and R. H. M. Hatley, “In vitro comparison of the effect of inhalation delay and flow rate on the emitted dose from three valved holding chambers,” *J. Aerosol Med. Pulm. Drug Deliv.*, vol. 27, no. SUPPL. 1, pp. 37–43, 2014, doi: 10.1089/jamp.2013.1061.
- [15] P. Csonka and L. Lehtimäki, “Valved holding chamber drug delivery is dependent on breathing pattern and device design,” *ERJ Open Res.*, vol. 5, no. 1, pp. 00158–02018, 2019, doi: 10.1183/23120541.00158-2018.
- [16] J. H. Wildhaber *et al.*, “Effect of electrostatic charge, flow, delay and multiple actuations on the in vitro delivery of salbutamol from different small volume spacers for infants,” *Thorax*, vol. 51, no. 10, pp. 985–988, 1996, doi: 10.1136/thx.51.10.985.
- [17] R. Falcão Oliveira *et al.*, “Efficiency of Valved Holding Chambers: Experimental

Full Dose Assessment Two-phase flow modelling in a venturi scrubber View project Design parameters of atomizers and spray flow simulation View project Efficiency of Valved Holding Chambers: Experimental ,” 2014, Accessed: May 07, 2018. [Online]. Available: <https://www.researchgate.net/publication/273110353>.

- [18] C. Wilson, N. Washington, and C. Washington, *Physiological Pharmaceutics*. 2010.
- [19] T. G. A. Patton, Kevin T, *Anatomy Ó Physiology*. 2013.
- [20] C. Kleinstreuer, Z. Zhang, and J. F. Donohue, “Targeted Drug-Aerosol Delivery in the Human Respiratory System,” *Annu. Rev. Biomed. Eng.*, vol. 10, no. 1, pp. 195–220, 2008, doi: 10.1146/annurev.bioeng.10.061807.160544.
- [21] A. McLuckie, *Respiratory Disease and its Management*, 1. Aufl. London: Springer Verlag London Limited, 2009.
- [22] M. K. Vernon, I. Wiklund, J. A. Bell, P. Dale, and K. R. Chapman, “What do we know about asthma triggers? A review of the literature,” *J. Asthma*, vol. 49, no. 10, pp. 991–998, 2012, doi: 10.3109/02770903.2012.738268.
- [23] T. Ferkol and D. Schraufnagel, “The global burden of respiratory disease,” *Ann. Am. Thorac. Soc.*, vol. 11, no. 3, pp. 404–406, 2014, doi: 10.1513/AnnalsATS.201311-405PS.
- [24] P. J. Barnes, J. M. Drazen, S. I. Rennard, and N. C. Thomson, *Asthma and COPD*, 2nd ed. San Diego: Elsevier Science & Technology, 2009.
- [25] “What you Need to Know about Asthma : Human N Health.” <https://humannhealth.com/what-you-need-to-know-about-asthma/341/> (accessed May 10, 2021).
- [26] B. R. Celli *et al.*, “Standards for the diagnosis and treatment of patients with COPD: A summary of the ATS/ERS position paper,” *Eur. Respir. J.*, vol. 23, no. 6, pp. 932–946, 2004, doi: 10.1183/09031936.04.00014304.

- [27] “Respiratory Diseases and Disorders | Respiratory Anatomy.”  
<https://www.visiblebody.com/learn/respiratory/diseases-and-disorders> (accessed May 10, 2021).
- [28] T. R. Des Jardins, G. G. Burton, and T. H. Phelps, *Clinical manifestations and assessment of respiratory disease*, 8th ed. .
- [29] J. A. Wedzicha, R. Singh, and A. J. Mackay, “Acute COPD exacerbations,” *Clin. Chest Med.*, vol. 35, no. 1, pp. 157–163, 2014, doi: 10.1016/j.ccm.2013.11.001.
- [30] R. Pauwels, S. Newman, and L. Borgström, “Airway deposition and airway effects of antiasthma drugs delivered from metered-dose inhalers,” *Eur Respir J*, vol. 10, no. 10, pp. 2127–2138, 1997, doi: 10.1183/09031936.97.10092127.
- [31] B. J. Lipworth and D. J. Clark, “Lung delivery of non-CFC salbutamol via small volume metal spacer and large volume plastic spacer devices compared with an open vent jet nebulizer.,” *Br. J. Clin. Pharmacol.*, vol. 45, no. 2, pp. 160–3, Feb. 1998, doi: 10.1046/J.1365-2125.1998.00648.X.
- [32] R. O. Williams, T. C. Carvalho, and J. I. Peters, “Influence of particle size on regional lung deposition - What evidence is there?,” *International Journal of Pharmaceutics*, vol. 406, no. 1–2, pp. 1–10, 2011, doi: 10.1016/j.ijpharm.2010.12.040.
- [33] A. Diameter, “Learn more about Aerodynamic Diameter GAS-CLEANING TECHNOLOGY,” 2001.
- [34] W. H. Finlay, “Motion of a single aerosol particle in a fluid,” *Mech. Inhaled Pharm. Aerosols*, pp. 21–52, Jan. 2019, doi: 10.1016/B978-0-08-102749-3.00003-8.
- [35] C. Darquenne, “Deposition Mechanisms,” *J. Aerosol Med. Pulm. Drug Deliv.*, vol. 33, no. 4, pp. 181–185, 2020, doi: 10.1089/jamp.2020.29029.cd.
- [36] “Microbial Cascade Impactor ~ California Tech Zone.”  
<https://catechzone.com/microbial-cascade-impactor/> (accessed Aug. 10, 2021).

- [37] J. Lay, "The effects of natural aggregates on the properties of concrete," *Adv. Concr. Technol.*, pp. 1–16, Jan. 2003, doi: 10.1016/B978-075065686-3/50284-6.
- [38] A. Petroff, A. Mailliat, M. Amielh, and F. Anselmet, "Aerosol dry deposition on vegetative canopies. Part I: Review of present knowledge," *Atmos. Environ.*, vol. 42, no. 16, pp. 3625–3653, 2008, doi: 10.1016/j.atmosenv.2007.09.043.
- [39] M. Lippmann, "Effects of fiber characteristics on lung deposition, retention, and disease," *Environ. Health Perspect.*, vol. 88, pp. 311–317, 1990, doi: 10.1289/ehp.9088311.
- [40] Y. S. Cheng, "Mechanisms of Pharmaceutical Aerosol Deposition in the Respiratory Tract," *AAPS PharmSciTech*, vol. 15, no. 3, pp. 630–640, 2014, doi: 10.1208/s12249-014-0092-0.
- [41] G. Crompton, "A brief history of inhaled asthma therapy over the last fifty years," *Prim. Care Respir. J.*, vol. 15, no. 6, pp. 326–331, 2006, doi: 10.1016/j.pcrj.2006.09.002.
- [42] R. F. Oliveira, S. Teixeira, J. C. Teixeira, L. F. Silva, and H. Antunes, "pMDI Sprays: Theory, Experiment and Numerical Simulation," in *Advances in Modeling of Fluid Dynamics*, InTech, 2012, pp. 255– 292.
- [43] T. S. Purewal and D. J. W. (David J. W. Grant, *Metered dose inhaler technology / edited by Tol S. Purewal and David J.W. Grant*. Boca Raton, Fla. : CRC Press, 1997.
- [44] A. M. Fonceca, W. G. Fox Ditcham, M. L. Everard, and S. Devadason, "Drug Administration by Inhalation in Children," *Kendig's Disord. Respir. Tract Child.*, pp. 257-271.e3, Jan. 2019, doi: 10.1016/B978-0-323-44887-1.00016-X.
- [45] S. P. Newman, "Principles of metered-dose inhaler design," *Respir. Care*, vol. 50, no. 9, pp. 1177–1190, 2005.
- [46] "Components of a pressurized metered-dose inhaler. (From Reference 135.) | Download Scientific Diagram." <https://www.researchgate.net/figure/Components->

of-a-pressurized-metered-dose-inhaler-From-Reference-135\_fig13\_5349250  
(accessed May 11, 2021).

- [47] A. Cripps, M. Riebe, M. Schulze, and R. Woodhouse, "Pharmaceutical transition to non-CFC pressurized metered dose inhalers.," *Respir. Med.*, vol. 94 Suppl B, pp. S3-9, 2000, [Online]. Available: <http://www.ncbi.nlm.nih.gov/pubmed/10919679>.
- [48] C. L. L. Dabt and T. F. C. Mdis, "The CFC to HFA Transition and Its Impact on Pulmonary Drug Development Safety Programs for the HFAs," *Respir. Care*, vol. 50, no. 9, pp. 1201–1208, 2005.
- [49] M. B. Dolovich and R. Dhand, "Aerosol drug delivery: Developments in device design and clinical use," *Lancet*, vol. 377, no. 9770, pp. 1032–1045, 2011, doi: 10.1016/S0140-6736(10)60926-9.
- [50] H. D. C. Smyth, V. P. Beck, D. Williams, and A. J. Hickey, "The Influence of Formulation and Spacer Device on the In Vitro Performance of Solution Chlorofluorocarbon-Free Propellant-Driven Metered Dose Inhalers," *AAPS PharmSciTech*, vol. 5, no. 1, 2004, Accessed: Mar. 07, 2018. [Online]. Available: <https://link.springer.com/content/pdf/10.1208%2Fpt050107.pdf>.
- [51] H. D. C. Smyth, "Multimodal particle size distributions emitted from HFA-134a solution pressurized metered-dose inhalers," *AAPS PharmSciTech*, vol. 4, no. 3, pp. 76–86, 2004, doi: 10.1208/pt040338.
- [52] B. J. Myatt *et al.*, "PDA and High Speed Image Analysis of HFA/Ethanol pMDI Aerosols: New Findings.," *Drug Deliv. to Lungs* 26, no. June, 2015.
- [53] M. Pirozynski and T. R. Sosnowski, "Inhalation devices: from basic science to practical use, innovative vs generic products," *Expert Opin. Drug Deliv.*, vol. 13, no. 11, pp. 1559–1571, 2016, doi: 10.1080/17425247.2016.1198774.
- [54] P. Sheth, M. D. Bertsch, C. L. Knapp, and P. B. Myrdal, "In vitro evaluation of nonconventional accessory devices for pressurized metered-dose inhalers," *Ann. Allergy, Asthma Immunol.*, vol. 113, no. 1, pp. 55–62, 2014, doi:

10.1016/j.anai.2014.04.006.

- [55] M. L. Everard, A. R. Clark, and A. D. Milner, "Drug delivery from holding chambers with attached facemask," *Arch. of Disease Child.*, vol. 67, pp. 580–585, 1992, Accessed: Apr. 18, 2018. [Online]. Available: <http://adc.bmj.com/content/archdischild/67/5/580.full.pdf>.
- [56] M. Nagel, J. N Schmidt, C. Doyle, V. M Varallo, and J. Mitchell, *DELAY TESTING OF VALVED HOLDING CHAMBERS (VHCs) WITH A NEW APPARATUS*. 2003.
- [57] R. F. Oliveira, A. C. Ferreira, S. F. Teixeira, J. C. Teixeira, and H. C. Marques, "PMDI spray plume analysis: A CFD study," *Lect. Notes Eng. Comput. Sci.*, vol. 3 LNECS, no. August, pp. 1883–1888, 2013.
- [58] E. Fröhlich and S. Salar-Behzadi, "Toxicological assessment of inhaled nanoparticles: Role of in vivo, ex vivo, in vitro, and in Silico Studies," *Int. J. Mol. Sci.*, vol. 15, no. 3, pp. 4795–4822, 2014, doi: 10.3390/ijms15034795.
- [59] C. Terzano, "Metered dose inhalers and spacer devices.," *Eur. Rev. Med. Pharmacol. Sci.*, vol. 3, no. 4, pp. 159–69, 1999, [Online]. Available: <http://www.ncbi.nlm.nih.gov/pubmed/11073122>.
- [60] C. TERZANO and F. MANNINO, "Aerosol characterization of three corticosteroid metered dose inhalers with volumatic holding chambers and metered dose inhalers alone at two inspiratory flow rates," *J. aerosol Med.*, vol. 12, no. 4, pp. 249–254, 1999.
- [61] J. H. Wildhaber *et al.*, "Electrostatic charge on a plastic spacer device influences the delivery of salbutamol," *Eur. Respir. J.*, vol. 9, no. 9, pp. 1943–1946, 1996, doi: 10.1183/09031936.96.09091943.
- [62] J. Suggett, M. Nagel, C. Doyle, H. Schneider, and J. Mitchell, "Use of Valved Holding Chambers Without Pre-Conditioning and the Influence of Anti-Static Materials," vol. 1, no. 3, pp. 3–6, 2014.
- [63] R. Rebelo, R. Oliveira, L. F. Silva, S. Teixeira, J. C. Teixeira, and H. Antunes,

“Further Developments on the CFD Flow Analysis Inside the Volumatic® Spacer,” in *Proc. 13th International Conference on Project Engineering*, 2010.

- [64] Z. Li, Y. Yuan, B. Guo, V. L. Varsegov, and J. Yao, “The Recirculation Zone Characteristics of the Circular Transverse Jet in Crossflow,” *Energies*, vol. 13, no. 12, p. 3224, 2020.
- [65] W. H. Fraser, “Flow recirculation in centrifugal pumps,” in *Proceedings of the 10th Turbomachinery Symposium*, 1981.
- [66] S. Sarkar, S. P. Peri, and B. Chaudhuri, “Investigation of multiphase multicomponent aerosol flow dictating pMDI-spacer interactions,” *Int. J. Pharm.*, vol. 529, no. 1–2, pp. 264–274, Aug. 2017, doi: 10.1016/j.ijpharm.2017.07.005.
- [67] R. F. Oliveira, S. F. C. F. Teixeira, L. F. Silva, J. C. F. Teixeira, and H. Antunes, “Computer Methods in Biomechanics and Biomedical Engineering Development of new spacer device geometry: a CFD study (Part I) Development of new spacer device geometry: a CFD study (Part I),” *Comput. Methods Biomech. Biomed. Engin.*, vol. 158, no. 10, 2012, doi: 10.1080/10255842.2011.563359.
- [68] N. Ogrodnik, V. Azzi, E. Sprigge, S. Fiset, and E. Matida, “Nonuniform deposition of pressurized metered-dose aerosol in spacer devices,” *J. Aerosol Med. Pulm. Drug Deliv.*, vol. 29, no. 6, pp. 490–500, 2016.
- [69] A. Yazdani, M. Normandie, M. Yousefi, M. S. Saidi, and G. Ahmadi, “Transport and deposition of pharmaceutical particles in three commercial spacer-MDI combinations,” *Comput. Biol. Med.*, vol. 54, pp. 145–155, 2014, doi: 10.1016/j.combiomed.2014.08.001.
- [70] W. H. Finlay and P. Zuberbuhler, “In vitro comparison of beclomethasone and salbutamol metered-dose inhaler aerosols inhaled during pediatric tidal breathing from four valved holding chambers,” *Chest*, vol. 114, no. 6, pp. 1676–1680, 1998, doi: 10.1378/chest.114.6.1676.
- [71] P. W. Barry and P. W. Barry C O, “Inhalational drug delivery from seven different spacer devices,” *Thorax*, vol. 51, pp. 835–840, 1996, Accessed: Mar. 07, 2018.



[Online]. Available: <http://thorax.bmj.com/content/thoraxjnl/51/8/835.full.pdf>.

- [72] M. J. Asmus, J. Liang, I. Coowanitwong, and G. Hochhaus, "In Vitro Performance Characteristics of Valved Holding Chamber and Spacer Devices with a Fluticasone Metered-Dose Inhaler," *Pharmacotherapy*, vol. 24, no. 2 I, pp. 159–166, 2004, doi: 10.1592/phco.24.2.159.33147.
- [73] S. Dissanayake, M. Nagel, E. Falaschetti, and J. Suggett, "Are valved holding chambers (VHCs) interchangeable? An in vitro evaluation of VHC equivalence," *Pulm. Pharmacol. Ther.*, vol. 48, no. July 2017, pp. 179–184, 2017, doi: 10.1016/j.pupt.2017.10.005.
- [74] H. Bisgaard, "A metal aerosol holding chamber devised for young children with asthma," *Eur. Respir. J.*, vol. 8, no. 5, pp. 856–860, 1995, doi: 10.1183/09031936.95.08050856.
- [75] G. A. Koelsche, "Aerosol therapy," *J. Allergy*, vol. 19, no. 1, pp. 47–57, 1948, doi: 10.1016/0021-8707(48)90076-8.
- [76] T. Ghazanfari, A. M. A. Elhissi, Z. Ding, and K. M. G. Taylor, "The influence of fluid physicochemical properties on vibrating-mesh nebulization," *Int. J. Pharm.*, vol. 339, no. 1–2, pp. 103–111, 2007, doi: 10.1016/j.ijpharm.2007.02.035.
- [77] S. Pedersen, "Inhalers and nebulizers: Which to choose and why," *Respir. Med.*, vol. 90, no. 2, pp. 69–77, 1996, doi: 10.1016/S0954-6111(96)90201-2.
- [78] A. Ari, "Jet, Ultrasonic, and Mesh Nebulizers: An Evaluation of Nebulizers for Better Clinical Outcomes," *Eurasian J. Pulmonol.*, vol. 16, no. 1, pp. 1–7, 2014, doi: 10.5152/ejp.2014.00087.
- [79] S. H. Moon, K. H. Chang, H. M. Park, B. J. Park, S. K. Yoo, and K. C. Nam, "Effects of driving frequency and voltage on the performances of vibrating mesh nebulizers," *Appl. Sci.*, vol. 11, no. 3, pp. 1–11, Feb. 2021, doi: 10.3390/app11031296.
- [80] "Handbook of Atomization and Sprays."

- [81] H. Hamishehkar, Y. Rahimpour, and Y. Javadzadeh, "The Role of Carrier in Dry Powder Inhaler," *Recent Adv. Nov. Drug Carr. Syst.*, 2012, doi: 10.5772/51209.
- [82] Y. N. and L. A., "Dry powder inhalers: A review," *Indo Glob. J. Pharm. Sci.*, vol. 3, no. 2, pp. 142–155, 2013, [Online]. Available: [http://www.embase.com/search/results?subaction=viewrecord&from=export&id=L372010549%5Cnhttp://www.iglobaljournal.com/wp-content/uploads/2013/12/6.-Yadav-Lohani-IGJPS-2013\\_Revised.pdf](http://www.embase.com/search/results?subaction=viewrecord&from=export&id=L372010549%5Cnhttp://www.iglobaljournal.com/wp-content/uploads/2013/12/6.-Yadav-Lohani-IGJPS-2013_Revised.pdf).
- [83] W. H. Finlay, *The mechanics of inhaled pharmaceutical aerosols : an introduction*. San Diego : Academic Press, 2001.
- [84] T. DP, "New devices for asthma," *J. Allergy Clin. Immunol.*, vol. 101, no. 2 Pt 2, 1998, doi: 10.1016/S0091-6749(98)70233-7.
- [85] J. H. Ferziger, M. Perić, and R. L. Street, *Computational methods for fluid dynamics*, vol. 3. Springer, 2002.
- [86] V. Thomée, "From finite differences to finite elements," *J. Comput. Appl. Math.*, vol. 128, no. 1–2, pp. 1–54, 2001, doi: 10.1016/s0377-0427(00)00507-0.
- [87] P. P. Kakade, N. Mishchiy, and A. V. Annapragada, "Computational fluid dynamics simulation of airflow and aerosol deposition in human lungs," *Annu. Int. Conf. IEEE Eng. Med. Biol. - Proc.*, vol. 2, pp. 1493–1494, 2002, doi: 10.1109/IEMBS.2002.1106501.
- [88] "ANSYS FLUENT 12.0 User's Guide - 6.2.2 Mesh Quality." <https://www.afs.enea.it/project/neptunius/docs/fluent/html/ug/node167.htm> (accessed May 31, 2021).
- [89] P. W. Longest and S. Vinchurkar, "Effects of mesh style and grid convergence on particle deposition in bifurcating airway models with comparisons to experimental data," *Med. Eng. Phys.*, vol. 29, no. 3, pp. 350–366, 2007, doi: 10.1016/j.medengphy.2006.05.012.
- [90] M. Yousefi, O. Pourmehran, M. Gorji-Bandpy, K. Inthavong, L. Yeo, and J. Tu,

- “CFD simulation of aerosol delivery to a human lung via surface acoustic wave nebulization,” *Biomech. Model. Mechanobiol.*, vol. 16, no. 6, pp. 2035–2050, 2017, doi: 10.1007/s10237-017-0936-0.
- [91] T. D. Canonsburg, “ANSYS CFX-Solver Modeling Guide,” vol. 15317, no. November, pp. 724–746, 2011.
- [92] J. Milenkovic, A. H. Alexopoulos, and C. Kiparissides, “Flow and particle deposition in the Turbuhaler: A CFD simulation,” *Int. J. Pharm.*, vol. 448, no. 1, pp. 205–213, 2013, doi: 10.1016/j.ijpharm.2013.03.004.
- [93] F. Greifzu, C. Kratzsch, T. Forgber, F. Lindner, and R. Schwarze, “Assessment of particle-tracking models for dispersed particle-laden flows implemented in OpenFOAM and ANSYS FLUENT,” <http://www.tandfonline.com/action/authorSubmission?journalCode=tcfm20&page=instructions>, vol. 10, no. 1, pp. 30–43, Jan. 2015, doi: 10.1080/19942060.2015.1104266.
- [94] D. Zuzio, J. L. Estivalezes, P. Villedieu, and G. Blanchard, “Numerical simulation of primary and secondary atomization,” *Comptes Rendus - Mec.*, vol. 341, no. 1–2, pp. 15–25, 2013, doi: 10.1016/j.crme.2012.10.003.
- [95] R. Falcão Oliveira and S. F. C F Teixeira, “Study of a Pressurized Metered-dose Inhaler Spray Parameters in Fluent™,” *Lect. Notes Eng. Comput. Sci.*, 2010, Accessed: May 07, 2018. [Online]. Available: <https://www.researchgate.net/publication/45534551>.
- [96] G. K. J. Kitscha, “breakup criteria for fluid particles,” *Multiph. Flow*, vol. 15, no. 4, pp. 573–588, 1989.
- [97] D. R. Gueldenbecher, C. López-Rivera, and P. E. Sojka, “Secondary atomization,” *Exp. Fluids*, vol. 46, no. 3, pp. 371–402, 2009, doi: 10.1007/s00348-008-0593-2.
- [98] Y. Chen *et al.*, “Aerodynamic breakup and secondary drop formation for a liquid metal column in a shock-induced cross-flow,” *AIAA SciTech Forum - 55th AIAA Aerosp. Sci. Meet.*, no. January, 2017, doi: 10.2514/6.2017-1892.

- [99] ANSYS, "ANSYS CFD-Solver Theory Guide. Release 14.0," vol. 15317, no. November, pp. 724–746, 2011, [Online]. Available: [http://www1.ansys.com/customer/content/documentation/140/cfx\\_thry.pdf](http://www1.ansys.com/customer/content/documentation/140/cfx_thry.pdf).
- [100] M. C. Fung, K. Inthavong, W. Yang, and J. Tu, "CFD modeling of spray atomization for a nasal spray device," *Aerosol Sci. Technol.*, vol. 46, no. 11, pp. 1219–1226, 2012, doi: 10.1080/02786826.2012.704098.
- [101] C. Kleinstreuer, H. Shi, and Z. Zhang, "Computational analyses of a pressurized metered dose inhaler and a new drug–aerosol targeting methodology," *J. aerosol Med.*, vol. 20, no. 3, pp. 294–309, 2007.
- [102] S. A. Solanki, D. R. Patel, K. B. Parikh, and G. Vasan, "Numerical models of diesel spray characteristics at secondary break up stage," *Int. J. Adv. Eng. Res. Stud. IJAERS*, vol. 2, pp. 1–4, 2013.
- [103] C. Walck and P. P. Group, "Hand-book on STATISTICAL for experimentalists," *October*, no. September, pp. 1–202, 2007.
- [104] A. Macías-García, E. M. Cuerda-Correa, and M. A. Díaz-Díez, "Application of the Rosin-Rammler and Gates-Gaudin-Schuhmann models to the particle size distribution analysis of agglomerated cork," *Mater. Charact.*, vol. 52, no. 2, pp. 159–164, 2004, doi: 10.1016/j.matchar.2004.04.007.
- [105] H. C. M. and J. C. T. Ricardo F. Oliveira, Senhorinha F. Teixeira, "Efficiency evaluation of VHC: a CFD comparison study at constant flow," in *International Conference on Mechanics, Fluid Mechanics, Heat and Mass Transfer*, 2014, Accessed: May 09, 2018. [Online]. Available: <http://inase.org/library/2014/interlaken/bypaper/MECH/MECH-07.pdf>.
- [106] A. Alonzo-García, C. del C. Gutiérrez-Torres, and J. A. Jiménez-Bernal, "Computational Fluid Dynamics in Turbulent Flow Applications," *Numer. Simul. - From Brain Imaging to Turbul. Flows*, no. August, 2016, doi: 10.5772/63831.
- [107] P. Majumdar, "Computational Fluid Dynamics Analysis of Turbulent Flow," *Comput. Fluid Dyn. Technol. Appl.*, 2012, doi: 10.5772/16284.

- [108] “ANSYS CFX-Solver Theory Guide,” vol. 15317, no. November, pp. 724–746, 2011.
- [109] M. Ilie, E. A. Matida, and W. H. Finlay, “Asymmetrical Aerosol Deposition in an Idealized Mouth with a DPI Mouthpiece Inlet,” *Aerosol Sci. Technol.*, vol. 42, no. 1, pp. 10–17, 2008, doi: 10.1080/02786820701777440.
- [110] M. A. Liebert, “Characterization of Regional and Local Deposition of Inhaled Aerosol Drugs in the Respiratory System by Computational Fluid and Particle Dynamics Methods,” *J. Aerosol Med.*, vol. 19, no. 3, pp. 329–343, 2006.
- [111] F. Menter, “Zonal Two Equation k- $\omega$  Turbulence Models For Aerodynamic Flows,” in *23rd Fluid Dynamics, Plasmadynamics, and Lasers Conference*, American Institute of Aeronautics and Astronautics, 1993.
- [112] F. R. Menter, “Two-equation eddy-viscosity turbulence models for engineering applications,” *AIAA J.*, vol. 32, no. 8, pp. 1598–1605, Aug. 1994, doi: 10.2514/3.12149.
- [113] B. Devolder, P. Troch, and P. Rauwoens, “Performance of a buoyancy-modified k- $\omega$  and k- $\omega$  SST turbulence model for simulating wave breaking under regular waves using OpenFOAM®,” vol. 138, no. August 2017, pp. 49–65, 2018, doi: 10.1016/j.coastaleng.2018.04.011.
- [114] Á. Farkas *et al.*, “Effect of delayed pMDI actuation on the lung deposition of a fixed-dose combination aerosol drug,” *Int. J. Pharm.*, vol. 547, no. 1–2, pp. 480–488, 2018, doi: 10.1016/j.ijpharm.2018.06.016.
- [115] P. W. Longest *et al.*, “Use of computational fluid dynamics deposition modeling in respiratory drug delivery,” *Expert Opin. Drug Deliv.*, vol. 16, no. 1, pp. 7–26, 2019, doi: 10.1080/17425247.2019.1551875.
- [116] P. W. Longest, M. Hindle, S. Das Choudhuri, and J. Xi, “Comparison of ambient and spray aerosol deposition in a standard induction port and more realistic mouth–throat geometry,” *Aerosol Sci.*, vol. 39, pp. 572–591, 2008, doi: 10.1016/j.jaerosci.2008.03.008.

- [117] H. D. s. . Karunaratne and L.-A. Tokheim, *Comparison of the influence of drag models in CFD simulation of particle mixing and segregation in a rotating cylinder*. 2017.
- [118] T. D. Canonsburg, "ANSYS CFD-Post User ' s Guide," vol. 15317, no. October, pp. 724–746, 2012.
- [119] T. Sapsis and G. Haller, "Instabilities in the dynamics of neutrally buoyant particles," *Phys. Fluids* 20, 017102, vol. 017102, no. November 2007, 2011, doi: 10.1063/1.2830328.
- [120] S. Wang, N. Ohmura, S. Wang, and N. Ohmura, "Dynamical Particle Motions in Vortex Flows Dynamical Particle Motions in Vortex Flows."
- [121] M. Dolovich and J. Mitchell, "Canadian Standards Association Standard CAN/CSA/Z264.1-02:2002: A New Voluntary Standard for Spacers and Holding Chambers Used with Pressurized Metered-Dose Inhalers," *Can. Respir. J.*, vol. 11, pp. 489–495, Nov. 2004, doi: 10.1155/2004/497946.
- [122] G. J. Newton, O. G. Raabe, and B. V. Mokler, "Cascade impactor design and performance," *J. Aerosol Sci.*, vol. 8, no. 5, pp. 339–347, 1977, doi: 10.1016/0021-8502(77)90021-0.
- [123] T. T. Mercer, M. I. Tillery, and G. J. Newton, "A multi-stage, low flow rate cascade impactor," *J. Aerosol Sci.*, vol. 1, no. 1, pp. 9–15, 1970, doi: 10.1016/0021-8502(70)90024-8.
- [124] M. Hata, B. Linfa, Y. Otani, and M. Furuuchi, "Performance evaluation of an Andersen cascade impactor with an additional stage for nanoparticle sampling," *Aerosol Air Qual. Res.*, vol. 12, no. 6, pp. 1041–1048, 2012, doi: 10.4209/aaqr.2012.08.0204.
- [125] S. L. Nixdorf, *UV-Vis Spectroscopy*. 2019.
- [126] "4.4: UV-Visible Spectroscopy - Chemistry LibreTexts."  
[https://chem.libretexts.org/Bookshelves/Analytical\\_Chemistry/Book%3A\\_Physical](https://chem.libretexts.org/Bookshelves/Analytical_Chemistry/Book%3A_Physical)

\_Methods\_in\_Chemistry\_and\_Nano\_Science\_(Barron)/04%3A\_Chemical\_Specialization/4.04%3A\_UV-Visible\_Spectroscopy (accessed Jun. 10, 2021).

- [127] G. Mahmood, "Turbine Blade Aerodynamics Sumanta Acharya."
- [128] A. D. Canonsburg, "ANSYS DesignXplorer User ' s Guide," vol. 15317, no. January, pp. 724–746, 2015.
- [129] D. Goldberg, "Genetic algorithms in optimization, search and machine learning," *Addison Wesley*. 1988.
- [130] K. Deb, *Multi-Objective Optimization using Evolutionary Algorithms Kalyanmoy*, vol. 16, no. 9. 2001.
- [131] Y. Ding, L. Chen, and K. Hao, *Bio-inspired optimization algorithms*, vol. 118. 2018.
- [132] Y. Tian, H. Wang, X. Zhang, and Y. Jin, "Effectiveness and efficiency of non-dominated sorting for evolutionary multi- and many-objective optimization," *Complex Intell. Syst.* 2017 34, vol. 3, no. 4, pp. 247–263, Sep. 2017, doi: 10.1007/S40747-017-0057-5.
- [133] H. Y. Alhammadi and J. A. Romagnoli, "Process design and operation: Incorporating environmental, profitability, heat integration and controllability considerations," *Comput. Aided Chem. Eng.*, vol. 17, no. C, pp. 264–305, Jan. 2004, doi: 10.1016/S1570-7946(04)80063-4.
- [134] J. Liu and X. Chen, "An improved NSGA-II algorithm based on crowding distance elimination strategy," *Int. J. Comput. Intell. Syst.*, vol. 12, no. 2, pp. 513–518, 2019, doi: 10.2991/IJCIS.D.190328.001.
- [135] B. Gavtash *et al.*, "Transient aerodynamic atomization model to predict aerosol droplet size of pressurized metered dose inhalers (pMDI)," *Aerosol Sci. Technol.*, vol. 51, no. 8, pp. 998–1008, 2017, doi: 10.1080/02786826.2017.1327121.
- [136] A. I. Khuri and S. Mukhopadhyay, "Response surface methodology," *Wiley Interdiscip. Rev. Comput. Stat.*, vol. 2, no. 2, pp. 128–149, 2010, doi:

10.1002/wics.73.

- [137] R. H. Myers, D. C. Montgomery, G. Geoffrey Vining, C. M. Borrer, and S. M. Kowalski, "Response Surface Methodology: A Retrospective and Literature Survey," *J. Qual. Technol.*, vol. 36, no. 1, pp. 53–78, 2004, doi: 10.1080/00224065.2004.11980252.
- [138] R. H. Myers, *Response surface methodology : process and product optimization using designed experiments / Raymond H. Myers, Douglas C. Montgomery, Christine M. Anderson-Cook.*, 4th ed. 2016.